Punjab University Journal of Mathematics (2025), 57(01), 50-89
https://doi.org/10.52280/pujm.2025.57(01)03

Computational Modeling of Casson Blood Flow in Symmetrically Stenosed Carotid Arteries Based on Finite Volume Scheme

Abdul Wahab
Department of Mathematics,
University of Management and Technology, Lahore, Pakistan

*Muhammad Imran Asjad
Department of Mathematics,
University of Management and Technology, Lahore, Pakistan

Kubra Anjum
Department of Medical Sciences,
Gujranwala Medical College, Gujranwala, 52250 Pakistan

Saraj Khan
Department of Mathematics,
University of Management and Technology, Lahore, Pakistan

*Corresponding Author
imran.asjad@umt.edu.pk

Received: 03 Febraury, 2025 / Accepted: 19 May, 2025 / Published online: 16 July, 2025

Abstract. Carotid atherosclerosis is a major contributor to cardiovascular morbidity and mortality, primarily due to plaque-induced arterial steno-sis. This study develops a patient-specific computational model of Casson blood flow in symmetrically stenosed carotid arteries using a finite volume method. Realistic artery geometries are reconstructed from MRI and CT imaging. The model indicates a significant pressure drop (from approxi-mately 917 Pa to -411 Pa) and an increase in blood velocity, peaking at 1.5 m/s within the stenosed region. Temperature gradients are noted along ar-terial walls due to frictional heating. The model is quantitatively validated with reference data and clinically confirmed by MRI diagnostics. The main findings of computational results further show that wall shear stress increases with stenosis severity, and recirculation zones intensify near the stenosis throat, potentially promoting plaque buildup. The Casson fluid model captures the non-Newtonian nature of blood effectively, while the finite volume scheme ensures stable and accurate numerical predictions. These insights advance the understanding of hemodynamic behavior in stenosed arteries and may aid in personalized treatment planning.

AMS (MOS) Subject Classification Codes: 35Q51; 35C07; 25U09; 35Q53
Key Words: CFD, Atherosclerosis, Carotid Artery, Casson Fluid, Ansys, Heart Attack, Blood Vessels, Finite Volume Method.

1. Introduction

Cardiovascular diseases, particularly those involving arterial stenosis, remain a leading cause of mortality worldwide. Among these, stenosis in the carotid artery is a critical concern due to its direct link to cerebrovascular events such as strokes. Hemodynamic changes caused by arterial narrowing significantly affect parameters like velocity, pressure, and wall shear stress, which are key factors in atherosclerotic plaque development and rupture. An estimated 31% of all fatalities globally are attributed to cardiovascular disorders, the majority of which are associated with atherosclerosis, a disorder that causes abnormal

hemodynamic conditions in arteries [5, 54]. The first indication of atherosclerosis, a silent, complex, and multifactorial disease [35, 38], is the formation of a plaque, which is caused by the buildup of lipids and immune cells in the artery wall. Regional biological, biomechanical, and systemic factors have been implicated in the development of this disease [23, 39, 55]. These variables have been shown to be mostly caused by local hemodynamics [29, 13, 51]. Wall Shear Stress (WSS) in particular is a well-known marker of coronary atherosclerosis progression. Low wall shear stress zones have long been recognized to be more susceptible to plaque development [6], yet high levels of WSS are linked to plaque instability. Furthermore, there is a substantial risk of thrombotic arterial and venous occlusions for COVID-19 individuals, according to recent studies. By taking into account the death rate caused by the virus itself thus far and its association with the development of atherosclerosis, the situation becomes significantly more complicated [52].

Any artery that becomes damaged has serious repercussions, but when coronary arteries are afflicted, the effects are significantly more severe. When fatty material accumulates in these arteries, it blocks blood flow to the heart muscle. As a result, there are less vital nutrients available, including oxygen and other nutrients required for healthy organ function. If the artery is completely blocked, the decreased blood flow may result in a heart attack or pain in the chest [40, 14]. Cardiovascular disease is commonly treated with balloon angioplasty combined with intracoronary stent insertion. Even though this technique keeps the artery open and restores blood flow, restenosis is nonetheless harmful [30]. Studying blood flow hemodynamics is essential because cardiovascular diseases have a wide range of impacts. Because of this, the majority of research efforts are focused on this area utilizing numerical or experimental methods. There are still certain disadvantages to these methods, even though there are a lot of experimental hemodynamic studies that use in vitro [24, 20], in vivo [15, 57], or ex vivo [25, 44] methodologies and have shown promising findings as stated in [42].

According to the aforementioned, computational methods have recently been considered the best technique by a number of studies [7] and have evolved into a practical tool for evaluating and predicting the onset of diseases as well as evaluating the efficacy of novel treatment devices. It is important to remember that computational models cannot completely replace experimental tests because they still struggle to accurately simulate natural blood flow [16]. However, they can overcome some of the limitations of experimental hemodynamic techniques by producing more realistic virtual models, obtaining fast and accurate results, and thoroughly testing various physiological conditions [31]. Recently, numerical simulations have gained popularity in computational atherosclerosis research because to their numerous advantages [58]. Numerical simulations require three fundamental steps to be fulfilled: pre-processing, solution, and post-processing. The initial step in solving the mathematical model is defining the geometry of the problem, after which mesh creation is carried out. This is followed by the specification of the flow physics model, the boundary conditions, and the fluid characteristics of blood. In the third phase, the outcomes of the problem's solution must be examined.

Scientists have utilized different calculations to display blood stream inside supply routes throughout the long term, with two primary methodologies: reasonable coronary

corridor models that were extrapolated from patient clinical information [8] or romanticized stenotic calculations with admired shapes, (for example, the half-circle [45], ellipsoid, gaussian condition, cosine capability, among others) [9, 43, 33].

Preceding laying out the blood qualities, the calculation not entirely set in stone to tackle the issue appropriately. The mind boggling blend of cells, proteins, lipoproteins, and particles that make up blood transports side-effects and supplements. The blood's consistency is expanded by red platelets, which influences the liquid's way of behaving. Besides, this supposition that is erroneous for the microcirculatory framework and in instances of stenosis, regardless of whether it is broadly acknowledged that considering blood as a Newtonian liquid is a fair estimate for huge veins. Red platelets tend to gather into rouleaux at low shear rates, which makes the non-Newtonian conduct more observable there. Different components that should be considered incorporate the cyclic idea of the heart siphon, which makes pulsatile conditions, and the versatile conduct saw in the supply route wall [17, 26].

Blood's versatility, non-Newtonian viscosity, liquid particles, and body powers are therapeutically huge attributes, despite the fact that they can be overlooked to make blood stream examination simpler [46]. The mechanical qualities of blood courses, physiological stream conditions, and blood rheology, among other mechanical and organic perspectives, all straightforwardly affect the exactness of CFD models used to foresee blood stream. Subsequently, an enormous number of concentrates in the writing recreate blood stream utilizing different limit conditions. Various prior examinations have utilized computational liquid elements (CFD) reenactment in three-layered models produced using physical clinical pictures to look at the blood stream in the carotid corridor [19]. The complicated design of the ailing carotid bifurcation and its impact on blood stream designs make studies utilizing patient-explicit calculations significant [56]. Late examination by Saxena et al. [47] utilized Dynamic Powerful Thermography (ADT) to recognize carotid vein stenosis. Lopes shockingly led an intensive survey of the writing on mathematical demonstrating of carotid corridors custom-made to individual patients.

Three essential classes might be recognized among the carotid vein CFD mathematical recreations in view of our appraisal of the writing. A laminar stream model or a choppiness model should be thought about first. Second, the consistency models are thought about utilizing either Newtonian, non-Newtonian, or both. Nearly talking, the carotid vein might have a stenotic, nonstenotic, or both structure.

Various examinations suggest ordering blood as a non-Newtonian liquid because of the critical variations in hemodynamic boundary values among Newtonian and non-Newtonian liquids. As per Bouteloup et al. [36], the non-Newtonian impacts might be overstated on the off chance that the non-Newtonian models don't observe moral rules. While most of past examination considered the laminar stream model, only one review utilized the K-choppiness model. Blood stream is attempted to be laminar as the processed Reynolds number is under 2000. Nonetheless, there is a decent opportunity that stream will move to a momentary or even fierce condition in cases with very stenosed calculations. Past CFD concentrates on that analyzed the hemodynamics of stenosed spaces additionally expected that the stream was laminar. Thusly, there is an examination void in this field for CFD mathematical recreation that utilizes a reasonable choppiness model to look at carotid conduits that are stenosed and those that are not. CFD is a useful instrument for grasping

the component of atherosclerosis. Physically precise CFD models and limit conditions got from in vivo imaging strategies are utilized to portray the job of hemodynamics and plaque development and movement in corridors [48].

Previously employed for qualitative validation, image-based CFD has evolved to quantitative validation and is now widely utilized in applied vascular research. A new development in CFD is the use of realistic models taken from ex vivo or in vivo imaging methods, which provide pictures from which the artery lumen is taken out and rebuilt to create a three-dimensional lumen geometry.

The hemodynamics of patient-explicit models were analyzed utilizing picture based CFD to exhibit the pertinence of CFD for stream field research. To anticipate future gamble for carotid sicknesses, the Navier-Stirs up condition is used related to clinical imaging to research the time-shifting stream in the normal carotid course bifurcation [59, 21, 1]. The connection between hemodynamic factors and atherosclerosis might be assessed by joining CFD and MR imaging to analyze stream designs [2, 10]. Utilizing reasonable models got from clinical imaging advancements like CT (Modernized Tomography) and X-ray is a new pattern in computational hemodynamics [3, 4]. Utilizing three-layered (3D) models made from physical clinical imaging and computational liquid elements (CFD) reenactment, this study explored the blood stream in the carotid corridor. To survey any clinical case and its course, the vein's construction and blood stream not entirely settled. How much pressure and tension on the plaque decides if happiness happens, and the specialist pursues a treatment choice in view of these qualities, which might include medicine, stents, or medical procedure. Perceive how the plaque searches in three aspects. Figured tomography (CT) or attractive reverberation imaging (X-ray) are utilized to screen and analyze the plaque. Then, a 3D model of the plaque is made to assist the specialist with the treatment plan. At long last, the model delivered from imaging is partitioned to get the objective locale, and 3D printing is utilized to reproduce the tension, power, and blood stream of the model.

Despite extensive studies on blood flow in human vessels, most previous research has modeled blood as a Newtonian or generalized fluid, overlooking its non-Newtonian properties under certain physiological conditions [27]. Particularly, when blood becomes significantly more viscous due to pathological factors, such as during stenosis, its behavior aligns more closely with a Casson fluid model. However, the effects of this rheological behavior on velocity profiles, pressure distribution, and temperature changes have not been thoroughly investigated. Moreover, computational fluid dynamics (CFD) has been widely employed for studying blood flow in stenosed vessels, but the influence of Casson fluid properties on key hemodynamic parameters and flow contours remains underexplored. This represents a critical gap, as understanding the impact of non-Newtonian behavior in such conditions is essential for accurate predictions of flow dynamics and potential clinical interventions [18, 22].

Recent advancements in computational fluid dynamics (CFD) have enabled detailed simulations of blood flow under varying physiological and pathological conditions. For instance, Attar et al. [53] (2024) developed CFD models based on MRI and CT scans to analyze blood flow behavior in atherosclerotic carotid arteries, offering high anatomical accuracy and insightful hemodynamic data. Likewise, Carvalho et al. [37] (2021) validated transient simulations of 3D-printed coronary artery models, bridging experimental and computational approaches to better understand flow dynamics in stenotic vessels. While

Newtonian models have been widely used, growing evidence suggests that they may not accurately reflect the rheological nature of blood, especially under diseased states. Blood exhibits non-Newtonian behavior, particularly in high-shear or high-viscosity scenarios, such as in stenosed arteries. The Casson fluid model offers a more realistic representation in such cases, accounting for yield stress and shear-thinning behavior, yet its impact on hemodynamic variables remains under explored. Blood is a complex, non-Newtonian fluid whose viscosity varies with shear rate. While many studies have employed Newtonian models for simplicity, these fail to capture the yield-stress and shear-thinning properties critical in diseased states. Gijsen et al. [34] (2020) demonstrated that using non-Newtonian models such as Casson or Carreau can significantly affect predicted wall shear stress and recirculation zones. Kumar et al. [49] (2022) investigated Casson fluid flow in a tapered artery and found enhanced accuracy in predicting pressure drop and flow reversal. Additionally, Pandey et al. [41] (2023) incorporated non-Newtonian rheology in pulsatile flow models and noted notable differences in flow resistance and temperature rise due to frictional effects. Moreover, the role of thermal effects in arterial blood flow has gained attention. Friction-induced heating, although often neglected, may contribute to vascular wall weakening. Chakraborty et al. [11] (2022) studied thermal gradients in stenosed arteries and highlighted their influence on endothelial shear and thermal damage risks.

Despite the valuable insights provided by this study, certain limitations must be acknowledged. Firstly, the simulation is conducted under the assumption of steady-state flow. However, in physiological conditions, blood flow is inherently pulsatile due to the cardiac cycle, and this unsteady behavior can influence flow separation and wall shear stress dynamics, especially in diseased arteries. Secondly, a two-dimensional (2D) arterial geometry is employed to reduce computational complexity. While this approach is beneficial for preliminary analysis, it may oversimplify the actual three-dimensional nature of blood vessels and neglect important secondary flow structures. Furthermore, the model utilizes an idealized, symmetric stenosis, which may not fully capture the complexity of irregular and asymmetric geometries typically observed in real patients. Another simplification is the assumption of rigid arterial walls, whereas actual arteries are compliant and interact with the blood flow dynamically. This fluid–structure interaction can affect pressure gradients and velocity profiles, particularly in the post-stenotic region. Lastly, the study exclusively employs the Casson fluid model to describe the non-Newtonian behavior of blood. While the Casson model is widely used and appropriate for certain conditions, alternative models like Carreau-Yasuda or Herschel–Bulkley could provide more accurate predictions under different flow regimes or shear rates.

This study addresses this gap by employing the Casson fluid model in a CFD framework to simulate blood flow through a stenosed carotid artery. Our work aims to analyze the influence of non-Newtonian viscosity on velocity profiles, pressure distributions, and thermal variations. By integrating realistic geometry from medical imaging and applying advanced CFD techniques, this study contributes to a deeper understanding of flow alterations due to stenosis and provides insights that may aid in clinical assessments and therapeutic strategies.

The Casson fluid model is chosen specifically for its ability to represent the yield stress behavior of blood, which becomes particularly significant in stenosed arteries where low

shear rates and cellular aggregation dominate. Unlike the Power-Law model, Casson includes a yield stress component that captures the transition from plug-like to shear flow, which is observed in regions of recirculation and low shear near plaque deposits. Although the Carreau model provides a detailed representation of blood's shear-thinning properties across a wide range, it introduces more complexity and parameters. The Casson model offers a practical balance between physiological accuracy and computational efficiency for simulating hemodynamics in moderately stenosed geometries.

In highly stenosed regions, local Reynolds numbers may exceed 2000, potentially inducing transition or turbulence. In this study, we primarily focused on developing a validated laminar flow model using the Casson fluid assumption, which sufficiently captures essential hemodynamic patterns in moderate stenosis cases. Nonetheless, we agree that turbulent or transitional effects could become significant, particularly near severe stenotic throats. We plan to incorporate turbulence models (e.g., k-ω SST) in future work to evaluate their influence on stress, velocity, and heat transfer predictions.

The present model focuses on peak systolic behavior using a quasi-steady approximation of pulsatile flow. Despite this simplification, the model accurately captures the key spatial hemodynamic variations relevant to clinical assessment.

1.1. **Advantages of this study and our model.**

(1) **Realistic Representation of Blood Flow:** The Casson fluid model, which accounts for the non-Newtonian behavior of blood in high-viscosity situations, is used in this work in contrast to conventional Newtonian models. As a result, blood flow may be simulated more accurately, especially in pathological circumstances like stenosis.

(2) **Comprehensive Hemodynamic Analysis:** The work uses CFD models to give extensive information on important hemodynamic parameters, including as temperature, pressure, and velocity distributions. Understanding disease development and treatment planning need the ability to recognize flow patterns and high-stress locations, which these studies can assist in identifying.

(3) **Enhanced Clinical Relevance:** Improved diagnostic precision and treatment approaches can result from an understanding of how blood behaves as a Casson fluid in stenosed disorders. For instance, it provides a better understanding of how blood flow adjusts to pathological changes, which might help with the design of stents, surgical procedures, or targeted medication delivery systems.

(4) **Improved Predictive Capabilities:** The Casson fluid model's use into CFD improves flow disturbance predictions, which are essential for determining the likelihood of consequences such vascular rupture, ischemia, or clot formation.

(5) **Temperature and Heat Transfer Analysis:** The investigation gains a new dimension with the incorporation of temperature effects. With possible uses in hyperthermia-based treatments or in understanding thermal damage during treatments, this can aid in the investigation of how temperature gradients affect blood flow and vessel walls in sick states.

(6) **Foundation for Future Research:** In cardiovascular studies, this model acts as a springboard for more research into non-Newtonian fluid dynamics. In biological

applications, it provides avenues for investigating pulsatile flows, more intricate geometries, and multi-physics interactions.

(7) **Tool for Personalized Medicine:** The approach may be modified to fit the unique data of each patient, allowing for customized simulations that take particular blood characteristics and vascular geometry into account. In the healthcare industry, precision medicine is becoming more and more popular.

2. METERIALS AND METHODS

In the next sub section, the size of carotid Artery is established. Moreover, a numerical approach is made along with the boundary restrictions which helped in proposing the mathematical equation.

2.1. **Reynolds Number Calculation.** In our study, the Reynolds number (Re) was calculated to determine whether the flow within the carotid artery model remained laminar or had the potential to transition into turbulent flow, particularly near the stenosis.

Reynolds Number Formula:

$$Re = \frac{\rho V D}{\mu}$$

Where:

- $\rho = 1060\,\text{kg/m}^3$ (blood density),
- $V = 0.5\,\text{m/s}$ (peak systolic velocity),
- $D = 0.006\,\text{m}$ (approximate carotid artery diameter),
- $\mu = 0.0035\,\text{Pa} \cdot \text{s}$ (effective Casson fluid viscosity under shear).

Substituting the values:

$$Re = \frac{1060 \times 0.5 \times 0.006}{0.0035} \approx 909$$

Thus, under physiological conditions and even at peak systole, $Re < 1000$, which supports the assumption of laminar flow.

2.2. **Model Construction.** The geometric model was constructed keeping in mind its application in pulsatile flow simulations, which better represent physiological blood flow dynamics. The model supports transient simulations with time-varying boundary conditions, particularly a sinusoidal inlet velocity profile representing a heart rate of 140 BPM, as implemented later using a User Defined Function (UDF).

2.3. **Acquisition of Image.** In the first place, images from MRI of a carotid artery with atherosclerosis are used to generate the visuals of normal and the abnormal carotid arteries in the form of two- dimensional model and helical CT scan images. For example, it is observed that the number of MRI images found, for a patient with 40% carotid artery stenosis, were 560 slices provided by the National Institute Healthcare (NIH). On the other hand, the number of CT images for a normal patient were 483 slices. Moreover, when a 55 years old female patient with 30% stenosis was diagnosed, 512 slices of CT images were provided. The schematic diagram illustrates the carotid artery cross-section, showing the arterial walls (outer layer) and the lumen where blood flows. An ultrasound probe is

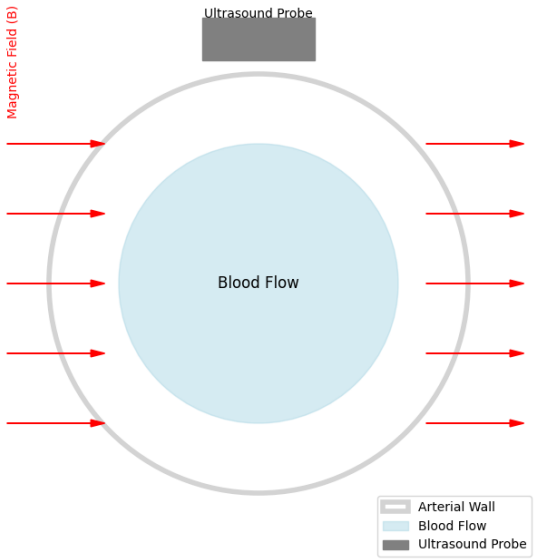

FIGURE 1. Magnetic field (B) is represented by arrows indicating direction and magnitude.

positioned above the artery, directing sound waves for imaging and measurement. Red arrows in the figure represent the magnetic field (B), indicating its direction and orientation relative to the artery, this is important because the interaction between the magnetic field and moving blood or tissues can influence signal behavior, depending on the study (e.g., magneto-acoustic or MR effects) shown in Figure 1 and blood flow analysis through the stenosis artery as shown in Figure 2.

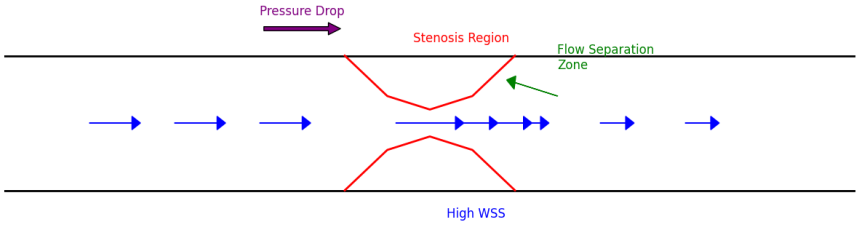

FIGURE 2. Schematic diagram of blood flow through a stenosed artery.

2.4. **2D-Modelling.** The piles of 2D Image data are considered to create a complete 2D model, 2D DOCTOR Software, a well-known V5 software, normally used for image processing of such models, made by Lexington based software company, Able software, is

used. The 2D model of the carotid artery was created by importing the Digital Imaging and Communications in Medicine (DICOM) images to the 2D DOCTOR, as shown in Figure 3. The inner and outer layers of the plaque as well as the arterial wall's borders were obtained by segmenting the pictures. Additionally, a 2D surface model was created using surface rendering. Because automatic segmentation was unable to detect the plaque in the carotid artery's 3D reconstruction, writers tended to mix automatic and manual segmentation approaches in order to improve results and detect the plaque more clearly. To get two more

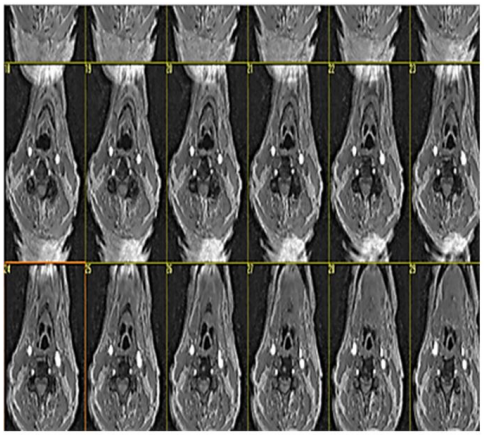

FIGURE 3. Imported visuals of DICOM.

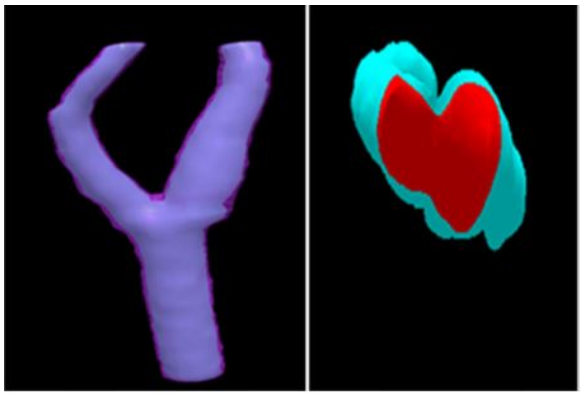

FIGURE 4. Visual of 2D segment of normal carotid artery.

examples with high plaque sizes, the plaque size was manually adjusted: normal (Figure 4) and abnormal (Figure 5). The same method was used on CT, as the data in Figure 6 illustrates, and both normal and pathological arteries with plaque showed improved results.

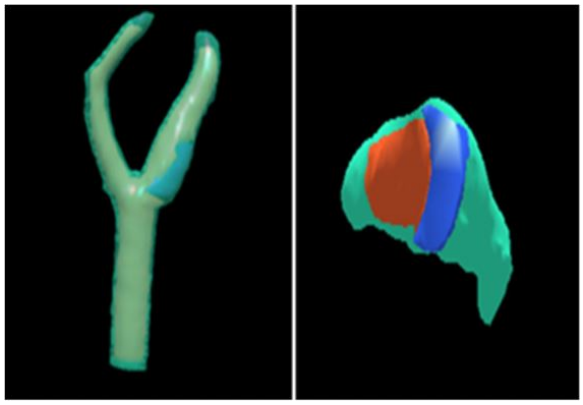

FIGURE 5. Visual of 2D segment of abnormal carotid artery.

2.5. **Converting the surface model to the volume model.** In order to get a solid geometry from the surface model, Rhinoceros (McNeel, Seattle, Washington) software is applied on the output of 2D Doctor program, mesh to an operation particularly, a Non-Uniform Rational Basis Splinenurb (NURBS) operation [28]. The display in the Figure 7 shows the profile of the plaque as a surface Figure 7 (a) and a model volume Figure 7 (b) as a consequence of using the MESHTONURB command. A mesh model and a NURBS

FIGURE 6. The CT scan visual of a 2D segment of normal and abnormal carotid artery.

surface model are distinct by the conversion using Rhinoceros Software with the help of the command of MESHTONURB, as seen in Figure 7 and effect of mesh refinement on maximum velocity and maximum static pressure in the carotid artery model are given in Table 1.

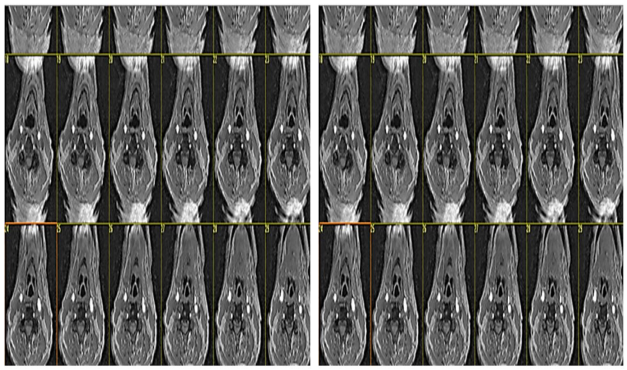

(A) Model as a surface. (B) Model as a volume.

FIGURE 7. Model as a surface and volume.

TABLE 1. Effect of mesh refinement on maximum velocity and maximum static pressure in the carotid artery model.

Mesh Size (No. of Elements)	Max Velocity (m/s)	Max Static Pressure (Pa)
118,538	1.47	905
345,000	1.49	910
602,225	1.50	917
703,353	1.50	918

2.6. **Mesh Independence and Computational Cost.** To ensure the accuracy of the 2D model, a preliminary mesh independence study was conducted during the model construction stage. Meshes with varying numbers of elements were tested, ranging from approximately 120,000 to 700,000 cells. It was observed that the velocity and pressure fields stabilized with a mesh size of around 600,000 elements, after which further mesh refinement produced negligible changes ($\leq 2\%$ variation). Therefore, the final model was built using a mesh of approximately 602,225 elements. The average computational time for a complete simulation per cardiac cycle was about 4 hours on a workstation with Intel i7 processor, 32 GB RAM, and NVIDIA GTX 1060 GPU. This mesh ensured a balance between computational efficiency and simulation accuracy.

2.7. **Simulation.** A renowned simulation integrating platform, ANSYS WorkbenchTM 17.0 is used in a situations when the 2D model of the carotid artery needs to simulate Fluid Structural Intention (FSI) [50]. FSI was used to a normal carotid artery after fluid and structural simulation was applied to a realistic contour of carotid artery. The model began simulating to ensure the findings produced are go with the work which was previously published by the author. In order to investigate Von Misses stress and strain, a basic structural model was created for the deformity of arterial wall. Additionally, a basic design is created for the arterial structure in both the non-stenotic (normal) and stenotic instances, and the velocity of the fluid (blood) and velocity profiles for pressure were examined using

a fluid analysis equipment. The 2D display developed by the researcher is to depict the targeted blood vessel in both non-stenotic and stenotic situations because it is necessary to simulate the flow of blood in the desired artery. The fluid and structure analysis of the carotid arteries in both cases was applied to geometries that were remodel by using the MRI images and the visuals provided by CT scan. The blood and the inlet and outflow boundary conditions Pere subjected to the simulation on the models having the characteristics dynamic material. Furthermore, in ANSYS, the velocity function on the inlet is established at the constant pressure of blood by on the outlets using UDF file and applied by Doppler ultrasonography. In the systolic phase, the velocity at the intake varies in a sinusoidal pattern, with a minimum velocity of 0.1 m/s for individuals with stenosis and a maximum velocity of 5 m/s for the sine wave. Each phase lasts 0.5 seconds, assuming that individuals with high blood pressure have a heart beat rate of 140 BPM, as shown in Figure 8. Although a time-varying sinusoidal inlet velocity is prescribed to approximate

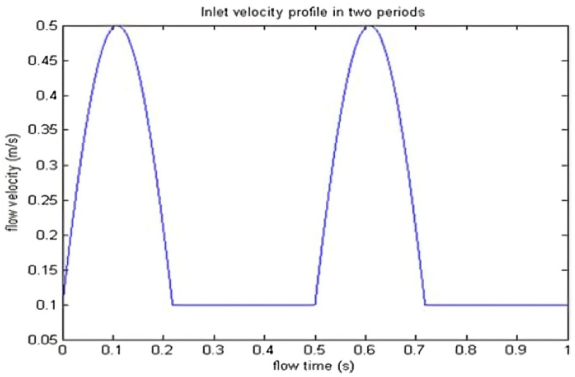

FIGURE 8. Sinusoidal velocity for a patient with 140 heartbeats/s.

physiological pulsatility, the simulation was treated as quasi-steady at selected time points (notably peak systole). This approach enables efficient analysis of spatial flow patterns and stress distributions during critical phases of the cardiac cycle. Future extensions of this work will involve fully transient pulsatile simulations across multiple cardiac phases to capture complete time-dependent hemodynamic effects.

2.8. **2D Printing.** After 2D reconstruction, a 2D visible model of the carotid artery was created to aid in more precise illness diagnosis.

3. GOVERNING EQUATIONS

The physiological flow of the ill and almost healthy models was simulated by solving the Navier-Stokes equations [3. 2 – 3. 4] conservation equations with finite volume are given in [32] and the continuity equation 3. 1 using ANSYS Fluent [9]. A turbulent blood flow is caused by different levels of stenosis, which lead to blockage and recirculation. The walls were subjected to a noslip boundary condition, assuming that the plaque was rigid. Then, blood is recalled to resemble the characteristics of blood in coronary veins by

being an incompressible, non-Newtonian liquid with a constant thickness of 1060 kg/m^3. Next, as stated in [43], are the controlling parameters for the three-layered mass and energy preservation associated with the blood stream:

$$\frac{\partial \tilde{u}}{\partial \tilde{x}} + \frac{\partial \tilde{v}}{\partial \tilde{y}} = 0. \tag{3. 1}$$

$$\tilde{u}\frac{\partial \tilde{u}}{\partial \tilde{x}} + \tilde{v}\frac{\partial \tilde{u}}{\partial \tilde{y}} = \tilde{v}\left(1 + \frac{1}{\beta}\right)\frac{\partial^2 \tilde{u}}{\partial \tilde{y}^2} - \frac{\sigma B_o^2 \tilde{u}}{\rho}. \tag{3. 2}$$

$$\tilde{u}\frac{\partial \tilde{T}}{\partial \tilde{x}} + \tilde{v}\frac{\partial \tilde{T}}{\partial \tilde{y}} = \alpha\frac{\partial^2 \tilde{T}}{\partial \tilde{y}^2} + \tilde{\tau}\left(\tilde{D}_B\frac{\partial \tilde{C}}{\partial \tilde{y}}\frac{\partial \tilde{T}}{\partial \tilde{y}} + \frac{\tilde{D}_T}{T_\infty}\left(\frac{\partial \tilde{T}}{\partial \tilde{y}}\right)^2\right). \tag{3. 3}$$

$$\tilde{u}\frac{\partial \tilde{C}}{\partial \tilde{x}} + \tilde{v}\frac{\partial \tilde{C}}{\partial \tilde{y}} = \tilde{D}_B\frac{\partial^2 \tilde{C}}{\partial \tilde{y}^2} + \frac{\tilde{D}_T}{T_\infty}\frac{\partial^2 \tilde{T}}{\partial \tilde{y}^2}. \tag{3. 4}$$

In the $x - axis$ and $y - axis$, the components of velocity are represented by $\tilde{u}$ and $\tilde{v}$, respectively. The viscosity coefficient value assumption is one element that might alter the interpretation of the equation. This study uses Casson's blood viscosity model, which permits the viscosity coefficient to change in response to the shear rate, therefore accounting for shear thinning.

3.1. **Finite Volume Method Approach.** Applying the Finite Volume Method (FVM) to the 2D PDEs involves the following steps:

- **Divide the Domain into Control Volumes**: The computational domain is divided into small, non-overlapping control volumes (CVs). The governing equations are integrated over these control volumes.
- **Approximate Fluxes at Control Volume Faces**: The flux terms (convective and diffusive) are evaluated at the faces of each control volume.
- **Discretize Each Equation**: Each PDE is discretized by applying the finite volume formulation, resulting in algebraic equations.

1. Continuity Equation. The continuity equation in 2D is:

$$\frac{\partial \tilde{u}}{\partial \tilde{x}} + \frac{\partial \tilde{v}}{\partial \tilde{y}} = 0$$

Step 1: Integration over Control Volume. Integrate over a control volume (CV) centered at point P with dimensions $\Delta x \times \Delta y$:

$$\int_{\text{CV}} \left(\frac{\partial \tilde{u}}{\partial \tilde{x}} + \frac{\partial \tilde{v}}{\partial \tilde{y}}\right) dA = 0$$

Using the divergence theorem:

$$\oint_{\text{CV}} \tilde{u}\,\hat{n}_x\,d\Gamma + \oint_{\text{CV}} \tilde{v}\,\hat{n}_y\,d\Gamma = 0$$

Step 2: Discretization of Fluxes. The fluxes across the CV faces are approximated:

$$\text{At east face: } \tilde{u}_E \Delta y, \quad \text{at west face: } \tilde{u}_W \Delta y$$

$$\text{At north face: } \tilde{v}_N \Delta x, \quad \text{at south face: } \tilde{v}_S \Delta x$$

The discretized continuity equation is:

$$\tilde{u}_E \Delta y - \tilde{u}_W \Delta y + \tilde{v}_N \Delta x - \tilde{v}_S \Delta x = 0$$

2. Momentum Equation. The momentum equation in 2D (in x-direction) is:

$$\tilde{u}\frac{\partial \tilde{u}}{\partial \tilde{x}} + \tilde{v}\frac{\partial \tilde{u}}{\partial \tilde{y}} = \nu \frac{\partial^2 \tilde{u}}{\partial \tilde{y}^2} - \frac{\sigma B_0^2 \tilde{u}}{\rho}$$

Step 1: Integration over Control Volume. Integrate over the control volume:

$$\int_{\text{CV}} \left(\tilde{u}\frac{\partial \tilde{u}}{\partial \tilde{x}} + \tilde{v}\frac{\partial \tilde{u}}{\partial \tilde{y}} \right) dA = \int_{\text{CV}} \nu \frac{\partial^2 \tilde{u}}{\partial \tilde{y}^2} dA - \int_{\text{CV}} \frac{\sigma B_0^2 \tilde{u}}{\rho} dA$$

Step 2: Convective Terms. Using Gauss's theorem:

$$\int_{\text{CV}} \tilde{u}\frac{\partial \tilde{u}}{\partial \tilde{x}} dA = \oint_{\text{CV}} \tilde{u}^2 \, \hat{n}_x \, d\Gamma$$

Discretize:

$$\tilde{u}\frac{\partial \tilde{u}}{\partial \tilde{x}} \approx \frac{(\tilde{u}_E^2 - \tilde{u}_W^2)}{\Delta x}$$

Similarly, for the y-direction:

$$\tilde{v}\frac{\partial \tilde{u}}{\partial \tilde{y}} \approx \frac{(\tilde{v}_N \tilde{u}_N - \tilde{v}_S \tilde{u}_S)}{\Delta y}$$

Step 3: Diffusive Terms. The diffusion term is:

$$\nu \frac{\partial^2 \tilde{u}}{\partial \tilde{y}^2} \approx \nu \frac{\tilde{u}_N - 2\tilde{u}_P + \tilde{u}_S}{\Delta y^2}$$

Step 4: Source Terms. The source term due to Lorentz force is:

$$-\frac{\sigma B_0^2 \tilde{u}_P}{\rho}$$

Step 5: Final Discretized Form.

$$a_P \tilde{u}_P = a_E \tilde{u}_E + a_W \tilde{u}_W + a_N \tilde{u}_N + a_S \tilde{u}_S + S_u$$

3. Energy Equation. The governing energy equation in 2D is given by:

$$\tilde{u}\frac{\partial \tilde{T}}{\partial \tilde{x}} + \tilde{v}\frac{\partial \tilde{T}}{\partial \tilde{y}} = \alpha \frac{\partial^2 \tilde{T}}{\partial \tilde{y}^2} + \tilde{\tau} \left(\tilde{D}_B \frac{\partial \tilde{C}}{\partial \tilde{y}} \frac{\partial \tilde{T}}{\partial \tilde{y}} + \frac{\tilde{D}_T}{T_\infty} \left(\frac{\partial \tilde{T}}{\partial \tilde{y}} \right)^2 \right)$$

Step 1: Integration Over Control Volume. Integrate the governing equation over the control volume (CV) centered at point P with dimensions $\Delta x \times \Delta y$:

$$\int_{\text{CV}} \left(\tilde{u}\frac{\partial \tilde{T}}{\partial \tilde{x}} + \tilde{v}\frac{\partial \tilde{T}}{\partial \tilde{y}} \right) dA = \int_{\text{CV}} \alpha \frac{\partial^2 \tilde{T}}{\partial \tilde{y}^2} dA + \int_{\text{CV}} \tilde{\tau} \left(\tilde{D}_B \frac{\partial \tilde{C}}{\partial \tilde{y}} \frac{\partial \tilde{T}}{\partial \tilde{y}} + \frac{\tilde{D}_T}{T_\infty} \left(\frac{\partial \tilde{T}}{\partial \tilde{y}} \right)^2 \right) dA$$

Step 2: Discretization of Convective Terms.

In the x-direction (Advection Term). For the advection term in the x-direction, we approximate as follows:

$$\int_{\text{CV}} \tilde{u}\frac{\partial \tilde{T}}{\partial \tilde{x}}\, dA \to \oint_{\text{CV}} \tilde{u}\tilde{T}\, \hat{n}_x\, d\Gamma$$

The fluxes across the faces are:

$$\text{Flux at east face: } \tilde{u}_E \tilde{T}_E \Delta y, \quad \text{Flux at west face: } \tilde{u}_W \tilde{T}_W \Delta y$$

Thus, the discretized form is:

$$\int_{\text{CV}} \tilde{u}\frac{\partial \tilde{T}}{\partial \tilde{x}}\, dA \approx \frac{\tilde{u}_E \tilde{T}_E - \tilde{u}_W \tilde{T}_W}{\Delta x} \Delta y$$

In the y-direction (Advection Term). Similarly, for the advection term in the y-direction:

$$\int_{\text{CV}} \tilde{v}\frac{\partial \tilde{T}}{\partial \tilde{y}}\, dA \to \oint_{\text{CV}} \tilde{v}\tilde{T}\, \hat{n}_y\, d\Gamma$$

The fluxes across the faces are:

$$\text{Flux at north face: } \tilde{v}_N \tilde{T}_N \Delta x, \quad \text{Flux at south face: } \tilde{v}_S \tilde{T}_S \Delta x$$

Thus, the discretized form is:

$$\int_{\text{CV}} \tilde{v}\frac{\partial \tilde{T}}{\partial \tilde{y}}\, dA \approx \frac{\tilde{v}_N \tilde{T}_N - \tilde{v}_S \tilde{T}_S}{\Delta y} \Delta x$$

Step 3: Discretization of Diffusive Terms. The diffusive term is:

$$\alpha \frac{\partial^2 \tilde{T}}{\partial \tilde{y}^2}$$

Using a central difference scheme, we approximate:

$$\frac{\partial^2 \tilde{T}}{\partial \tilde{y}^2} \approx \frac{\tilde{T}_N - 2\tilde{T}_P + \tilde{T}_S}{\Delta y^2}$$

Substituting this into the integral:

$$\int_{\text{CV}} \alpha \frac{\partial^2 \tilde{T}}{\partial \tilde{y}^2}\, dA \approx \alpha \frac{\tilde{T}_N - 2\tilde{T}_P + \tilde{T}_S}{\Delta y^2} \Delta x \Delta y$$

Step 4: Discretization of Source Terms. The source term is:

$$\tilde{\tau}\left(\tilde{D}_B\frac{\partial\tilde{C}}{\partial\tilde{y}}\frac{\partial\tilde{T}}{\partial\tilde{y}}+\frac{\tilde{D}_T}{T_\infty}\left(\frac{\partial\tilde{T}}{\partial\tilde{y}}\right)^2\right)$$

First Source Term:

$$\tilde{D}_B\frac{\partial\tilde{C}}{\partial\tilde{y}}\frac{\partial\tilde{T}}{\partial\tilde{y}}$$

Using finite differences, we approximate:

$$\frac{\partial\tilde{C}}{\partial\tilde{y}}\approx\frac{\tilde{C}_N-\tilde{C}_S}{\Delta y},\quad \frac{\partial\tilde{T}}{\partial\tilde{y}}\approx\frac{\tilde{T}_N-\tilde{T}_S}{\Delta y}$$

Substitute into the integral:

$$\tilde{D}_B\frac{\partial\tilde{C}}{\partial\tilde{y}}\frac{\partial\tilde{T}}{\partial\tilde{y}}\approx\tilde{D}_B\frac{(\tilde{C}_N-\tilde{C}_S)(\tilde{T}_N-\tilde{T}_S)}{\Delta y^2}$$

Second Source Term:

$$\frac{\tilde{D}_T}{T_\infty}\left(\frac{\partial\tilde{T}}{\partial\tilde{y}}\right)^2\approx\frac{\tilde{D}_T}{T_\infty}\frac{(\tilde{T}_N-\tilde{T}_S)^2}{\Delta y^2}$$

The total source term becomes:

$$\int_{\text{CV}}\text{Source Terms}\,dA\approx\tilde{\tau}\Delta x\left(\tilde{D}_B\frac{(\tilde{C}_N-\tilde{C}_S)(\tilde{T}_N-\tilde{T}_S)}{\Delta y^2}+\frac{\tilde{D}_T}{T_\infty}\frac{(\tilde{T}_N-\tilde{T}_S)^2}{\Delta y^2}\right)$$

Step 5: Assemble Final Discretized Equation. The final discretized energy equation at the control volume is:

$$\frac{\tilde{u}_E\tilde{T}_E-\tilde{u}_W\tilde{T}_W}{\Delta x}\Delta y+\frac{\tilde{v}_N\tilde{T}_N-\tilde{v}_S\tilde{T}_S}{\Delta y}\Delta x=\alpha\frac{\tilde{T}_N-2\tilde{T}_P+\tilde{T}_S}{\Delta y^2}\Delta x\Delta y+\text{Source Terms}$$

Simplified, the final form is:

$$a_P\tilde{T}_P=a_E\tilde{T}_E+a_W\tilde{T}_W+a_N\tilde{T}_N+a_S\tilde{T}_S+S_T$$

Where the coefficients are:

$$a_E=\frac{\tilde{u}_E\Delta y}{\Delta x},\quad a_W=\frac{\tilde{u}_W\Delta y}{\Delta x},\quad a_N=\frac{\tilde{v}_N\Delta x}{\Delta y},\quad a_S=\frac{\tilde{v}_S\Delta x}{\Delta y}$$

The source term S_T is given by:

$$S_T=\tilde{\tau}\Delta x\left(\tilde{D}_B\frac{(\tilde{C}_N-\tilde{C}_S)(\tilde{T}_N-\tilde{T}_S)}{\Delta y^2}+\frac{\tilde{D}_T}{T_\infty}\frac{(\tilde{T}_N-\tilde{T}_S)^2}{\Delta y^2}\right)$$

2. Concentration Equation. The governing concentration equation in 2D is given by:

$$\tilde{u}\frac{\partial \tilde{C}}{\partial \tilde{x}} + \tilde{v}\frac{\partial \tilde{C}}{\partial \tilde{y}} = \tilde{D}_B \frac{\partial^2 \tilde{C}}{\partial \tilde{y}^2} + \frac{\tilde{D}_T}{T_\infty}\frac{\partial^2 \tilde{T}}{\partial \tilde{y}^2}$$

Where: - $\tilde{C}$ is the concentration, - $\tilde{D}_B$ is the diffusivity of the substance, - $\tilde{D}_T$ is the thermal diffusivity, - T_∞ is the reference temperature.

Step 1: Integration Over Control Volume. The first step in applying the finite volume method is to integrate the governing equation over the control volume (CV). Let the control volume be centered at point P with dimensions $\Delta x \times \Delta y$. The integral of the equation over the control volume is:

$$\int_{\text{CV}} \left(\tilde{u}\frac{\partial \tilde{C}}{\partial \tilde{x}} + \tilde{v}\frac{\partial \tilde{C}}{\partial \tilde{y}} \right) dA = \int_{\text{CV}} \tilde{D}_B \frac{\partial^2 \tilde{C}}{\partial \tilde{y}^2} dA + \int_{\text{CV}} \frac{\tilde{D}_T}{T_\infty}\frac{\partial^2 \tilde{T}}{\partial \tilde{y}^2} dA$$

Step 2: Discretization of Convective Terms. We begin by discretizing the convective terms in the x- and y-directions.

In the x-direction (Advection Term). For the advection term in the x-direction, we apply Gauss's theorem to convert the volume integral into surface integrals:

$$\int_{\text{CV}} \tilde{u}\frac{\partial \tilde{C}}{\partial \tilde{x}}\, dA \to \oint_{\text{CV}} \tilde{u}\tilde{C}\, \hat{n}_x\, d\Gamma$$

The fluxes across the control volume faces are:

$$\text{Flux at east face: } \tilde{u}_E \tilde{C}_E \Delta y, \quad \text{Flux at west face: } \tilde{u}_W \tilde{C}_W \Delta y$$

Thus, the discretized form for the x-direction is:

$$\int_{\text{CV}} \tilde{u}\frac{\partial \tilde{C}}{\partial \tilde{x}}\, dA \approx \frac{\tilde{u}_E \tilde{C}_E - \tilde{u}_W \tilde{C}_W}{\Delta x}\Delta y$$

In the y-direction (Advection Term). Similarly, for the advection term in the y-direction:

$$\int_{\text{CV}} \tilde{v}\frac{\partial \tilde{C}}{\partial \tilde{y}}\, dA \to \oint_{\text{CV}} \tilde{v}\tilde{C}\, \hat{n}_y\, d\Gamma$$

The fluxes across the control volume faces are:

$$\text{Flux at north face: } \tilde{v}_N \tilde{C}_N \Delta x, \quad \text{Flux at south face: } \tilde{v}_S \tilde{C}_S \Delta x$$

Thus, the discretized form for the y-direction is:

$$\int_{\text{CV}} \tilde{v}\frac{\partial \tilde{C}}{\partial \tilde{y}}\, dA \approx \frac{\tilde{v}_N \tilde{C}_N - \tilde{v}_S \tilde{C}_S}{\Delta y}\Delta x$$

Step 3: Discretization of Diffusive Terms. The diffusive term is:

$$\tilde{D}_B \frac{\partial^2 \tilde{C}}{\partial \tilde{y}^2}$$

Using a central difference scheme for the second derivative:

$$\frac{\partial^2 \tilde{C}}{\partial \tilde{y}^2} \approx \frac{\tilde{C}_N - 2\tilde{C}_P + \tilde{C}_S}{\Delta y^2}$$

Substituting this into the integral:

$$\int_{\text{CV}} \tilde{D}_B \frac{\partial^2 \tilde{C}}{\partial \tilde{y}^2}\, dA \approx \tilde{D}_B \frac{\tilde{C}_N - 2\tilde{C}_P + \tilde{C}_S}{\Delta y^2} \Delta x \Delta y$$

Thermal Diffusion Term. The second term involves thermal diffusion:

$$\frac{\tilde{D}_T}{T_\infty} \frac{\partial^2 \tilde{T}}{\partial \tilde{y}^2}$$

Again, using central differences for the second derivative:

$$\frac{\partial^2 \tilde{T}}{\partial \tilde{y}^2} \approx \frac{\tilde{T}_N - 2\tilde{T}_P + \tilde{T}_S}{\Delta y^2}$$

Substituting this into the integral:

$$\int_{\text{CV}} \frac{\tilde{D}_T}{T_\infty} \frac{\partial^2 \tilde{T}}{\partial \tilde{y}^2}\, dA \approx \frac{\tilde{D}_T}{T_\infty} \frac{\tilde{T}_N - 2\tilde{T}_P + \tilde{T}_S}{\Delta y^2} \Delta x \Delta y$$

Step 4: Discretization of Source Terms. There may be additional source terms in the equation. In this case, no additional source terms are specified for the concentration equation, but they would be handled similarly by discretizing the integrals over the control volume.

Step 5: Assemble Final Discretized Equation. The final discretized concentration equation at the control volume is:

$$\frac{\tilde{u}_E \tilde{C}_E - \tilde{u}_W \tilde{C}_W}{\Delta x} \Delta y + \frac{\tilde{v}_N \tilde{C}_N - \tilde{v}_S \tilde{C}_S}{\Delta y} \Delta x = \tilde{D}_B \frac{\tilde{C}_N - 2\tilde{C}_P + \tilde{C}_S}{\Delta y^2} \Delta x \Delta y + \frac{\tilde{D}_T}{T_\infty} \frac{\tilde{T}_N - 2\tilde{T}_P + \tilde{T}_S}{\Delta y^2} \Delta x \Delta y$$

Simplified, the final form is:

$$a_P \tilde{C}_P = a_E \tilde{C}_E + a_W \tilde{C}_W + a_N \tilde{C}_N + a_S \tilde{C}_S + S_C$$

Where the coefficients are:

$$a_E = \frac{\tilde{u}_E \Delta y}{\Delta x}, \quad a_W = \frac{\tilde{u}_W \Delta y}{\Delta x}, \quad a_N = \frac{\tilde{v}_N \Delta x}{\Delta y}, \quad a_S = \frac{\tilde{v}_S \Delta x}{\Delta y}$$

The source term S_C is:

$$S_C = \tilde{D}_B \frac{\tilde{C}_N - 2\tilde{C}_P + \tilde{C}_S}{\Delta y^2} \Delta x \Delta y + \frac{\tilde{D}_T}{T_\infty} \frac{\tilde{T}_N - 2\tilde{T}_P + \tilde{T}_S}{\Delta y^2} \Delta x \Delta y$$

The factors in the situation incorporate the compelling thickness (μ_{eff}), viscosity at zero shear rates (μ_0), viscosity at boundless shear rate (μ_∞), time steady (λ), shear rate ($\dot{\gamma}$), and power-regulation list (n).

$$\mu_{\text{eff}}(\dot{\gamma}) = \mu_\infty + \frac{\mu_0 - \mu_\infty}{1 + (\lambda\dot{\gamma})^2}^{n-1} \tag{3. 5}$$

At the point when the second deviatoric stress invariant surpasses a basic worth, malleable materials start to come up short, as indicated by the von Mises yield measures, likewise called the Greatest Twisting Energy Hypothesis of Disappointment. This thought is an essential piece of pliancy hypothesis and is best pertinent to flexible materials, like specific metals. Von Mises pressure (σ_{Mises}) is often utilized by specialists to evaluate a plan's capacity to support a heap state. The plan is thought of as fruitless if the von Mises pressure surpasses the strength of the material (σ_{yld}). To learn on the off chance that the conduit wall or plaque can endure worry about a specific edge, this study utilizes von Mises anxiety. The von Mises pressure conditions for the administering conditions in this work are:

$$\sigma_{\text{Mises}} = \sqrt{\frac{(\sigma_1 - \sigma_2)^2}{2} + \frac{(\sigma_1 - \sigma_3)^2}{2} + \frac{(\sigma_2 - \sigma_3)^2}{2}} = \sigma_{\text{yld}}$$

The stress value σ_{yld} is equal to the tensile yield strength T in the governing equation. Since the compressive yield strength C is not taken into account in this equation, T and C are equal. By determining if the material's von Mises stress exceeds its yield strength, the failure condition is identified. The failure condition can be stated more simply as follows:

$$\sigma_{\text{Mises}} > \sigma_{\text{yld}}$$

The material is deemed to have failed if the von Mises stress σ_{Mises} is greater than the yield strength σ_{yld}.

Following the fulfillment of the liquid examination of blood, the anxiety on the vein wall are inspected utilizing a one-way collaboration between the liquid and the construction. The course wall's primary examination utilizes versatile and hyperelastic attributes. The limited component strategy is utilized to ascertain stresses. Expecting a pulse of 140 beats each moment, a sine wave with a greatest speed of 0.5 m/s and a base speed of 0.1 m/s is utilized during the systolic stage. The speed profile of the Sinnottet model, which is remembered to imitate pulsatile blood stream, is numerically portrayed by Eq. 3. 5 , [12]:

$$V_{\text{inlet}}(t) = \begin{cases} 0.5 \sin\left[4\pi(t + 0.0160236)\right], & 0.5n < t \leq 0.5n + 0.218 \\ 0.1, & 0.5n + 0.218 < t \leq 0.5(n+1) \end{cases}$$

4. Computational Mesh

The designs are made using the 2D Doctor Program, and the simulation findings reported in this research are carries out using the ANSYS simulator, as seen in Figure 9. A section of the carotid artery with and without stenosis are studies in physiological settings, and the results are divided into two categories: fluid analysis and structural analysis. It should be noted that no processing method is applied to the images.

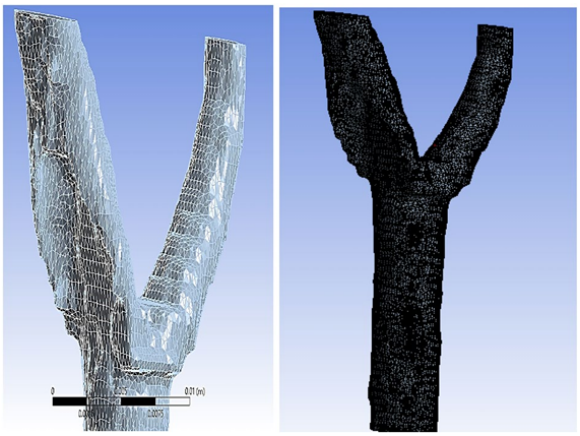

FIGURE 9. Blood geometry complying with the meshing process.

4.1. **Fluid Dynamics Analysis.** Different models is utilize to examine liquid stream. A couple is hand-attracted to work on the blood recreation, while others are exact reproductions from patient X's CT and X-ray pictures. Reproduction runs for both typical and strange stream designs are directed with the assumption that blood is an incompressible liquid to get an expansive information on the hemodynamics of ICA close to its bifurcation.

4.2. **Mesh Independent Study and Test Analysis.** Software that is sold commercially this geometric model is meshed using ANSYS Workbench. It has been stated that the fineness range for the two different meshes is between 118,538 and 703,353. Five simulations with three different grid sizes are done in order to identify the most realistic grid size. The meshes ranged from 118,538 to 703,353 elements. A mesh containing 602,225 elements was selected based on a balance of computational cost and solution accuracy. The mesh convergence study demonstrated less than 3% variation in pressure and velocity outputs between this and the finest grid, indicating a stable and accurate solution. Further refinement offered negligible accuracy improvement while increasing simulation time substantially. The mesh file is then loaded into the commercial application ANSYS Fluent, and 1000 testing cycles are carried out. For further investigation, the ultimate grid will consist of 602,225 components. A mesh independence study is performed using four mesh densities, and results for average velocity and wall shear stress are analyzed. It is observed that beyond Mesh 3 (51,446 elements), the changes in both parameters became negligible, indicating numerical convergence as shown in Figure 10. Therefore, Mesh 3 is selected for all further simulations as it provided a good balance between accuracy and computational cost.

5. BOUNDARY CONDITIONS

In this study, appropriate boundary conditions are defined to simulate blood flow through symmetrically stenosed carotid arteries using a finite volume method in ANSYS Fluent.

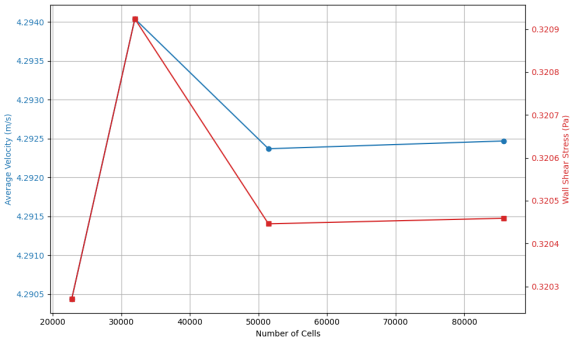

FIGURE 10. Mesh independence test analysis.

- **Inlet Boundary Condition:** A parabolic velocity profile is prescribed at the artery inlet to represent fully developed laminar blood flow. The maximum inlet velocity is based on clinical data, ranging from 0.1 m/s to 0.5 m/s depending on patient-specific factors. The inlet blood temperature is set to 310 K (37°C), representing physiological conditions.
- **Outlet Boundary Condition:** The outlet is modeled with a constant pressure condition (zero gauge pressure), allowing natural outflow and pressure gradient formation along the artery.
- **Wall Boundary Condition:** A no-slip boundary condition is applied on arterial walls, meaning the blood velocity is zero at the wall surface. The arterial wall is considered rigid and impermeable. For thermal analysis, either a constant wall temperature or specified heat flux condition is applied to assess heat transfer between blood and arterial tissue.
- **Symmetry Conditions:** If axisymmetric geometry is assumed in simplified 2D models, symmetry boundary conditions are applied to reduce computational complexity.

These boundary conditions ensure physiological accuracy of the model and enable detailed investigation of hemodynamic behavior in both healthy and stenosed regions.

5.1. **Computational readings for carotid stenosed artery.** In the process of meshing a healthy coronary artery, the software typically displays information such as the number of cells or elements, faces of elements, and total nodes generated to represent the arterial geometry accurately. This data helps to ensure an appropriate mesh resolution for computational simulations or analysis as given in Table 2.

TABLE 2. Data of mesh size

Cells	Faces	Nodes
2156	3456	1301

Software frequently offers mesh quality statistics, such as aspect ratio, orthogonality, and

element skewness, throughout the meshing process to evaluate the mesh's quality. For precise and trustworthy computer simulations or assessments of the coronary artery, this information is essential as given in Table 3.

TABLE 3. Data of mesh quality

Name	Type	Main Orthogonal Quality	Max Aspect Ratio
Fluid domain	Mixed Cell	0.041772624	73.693761

Software might also show the coronary artery models is given in Table 4 that were created in addition to mesh quality information. With the use of visualization and further analysis, these models, which depict the geometric structure of the artery, help to clarify arterial anatomy and pathophysiology.

TABLE 4. Models

Model	Setting
Space	2-D
Time	Steady
Viscous	Laminar
Heat Transfer	Abled

Data on material values utilized in the simulation are included in the proposed model along with reference values for comparison is given in Table 5 and Table 6. Elasticity, density, and viscosity are among the material variables that are included in this list since they are crucial for correctly depicting how the coronary artery behaves in various scenarios. The correctness and dependability of the model for modeling physiological or pathological events may be verified by comparing these results with reference data.

Elasticity, density, and viscosity are among the material variables that are included in

TABLE 5. Data of material properties

Fluid	Non-Newtonian
Density	1060 kgm^{-3}
Specific Heat	4182 $Jkg^{-1}K^{-1}$
Thermal Conductivity	0.6 $Wm^{-1}K^{-1}$
Viscosity	0.001003 $kgm^{-1}s^{-1}$
Molecular Weight	18.0152 $kgk^{-1}mol^{-1}$
Solid	Aluminum
Density	2719 kgm^{-3}
Specific Heat	1006.43 $Jkg^{-1}K^{-1}$
Thermal Conductivity	0.0242 $Wm^{-1}K^{-1}$

this list since they are crucial for correctly depicting how the coronary artery behaves in

various scenarios. The correctness and dependability of the model for modeling physiological or pathological events may be verified by comparing these results with reference data. The coronary artery model simulation or analysis's state of completion is indicated by the

TABLE 6. Data of reference values

Area	1 m^2
Density	1060 kgm^{-3}
Enthalpy	10 Jkg^{-1}
Length	1m
Pressure	80 Pa
Temperature	310 K
Velocity	0.75 ms^{-1}
Viscosity	$1.7894e^{-05}kgm^{-1}s^{-1}$
Ratio of specific heats	1.4
Yplus for heat transfer Coefficient	300
Reference Zone	fluid domain

solution status, which is given in Table 7 and graphically representation of convergence is shown in Figure 6 . It assists in monitoring the computing procedure, guaranteeing accurate model processing and timely resolution of any problems.

TABLE 7. Solution Status

Equations	**Value**	**Absolute Criteria**	**Convergence Status**
Continuity	0.2786517	$1e^{-06}$	Converged
x-velocity	0.0005115362	$1e^{-06}$	Converged
y-velocity	0.0005205321	$1e^{-06}$	Converged
Energy	$1.420451e^{-5}$	$1e^{-12}$	Converged

6. RESULTS AND DISCUSSION

In the Figure 11, significant differences in pressure values are found throughout the stenosed carotid artery segment when static pressure contours and pathlines are analyzed. The static pressure at the entrance is found to be quite high, at around $9.17 \times 10^2 Pa$ (red), which represents the blood flow's usual pressure prior to running into the stenosis. However, static pressure drastically drops when blood flows through the stenosed area, lowering to a minimum of around $-4.11 \times 10^2 Pa$ (dark blue). This dramatic drop is explained by stenosis, which narrows the artery lumen and raises blood flow velocity because of Bernoulli's equation and the principle of conservation of mass. This concept states that an increase in velocity results in a comparable. The static pressure starts to marginally recover downstream of the stenosis, reaching a value of around $2.53 \times 10^2 Pa$ (light blue). The reason for this recovery is that blood flow slows down when it leaves the stenosed area and re-enters a larger portion of the artery, where it stabilizes. High shear stress and turbulence

in the narrow zone cause considerable energy dissipation and pressure decrease, which is consistent with the hemodynamic consequences of stenosis and the observed pressure reductions. As the turbulence decreases, the tiny increase in pressure downstream indicates a partial restoration of laminar flow.

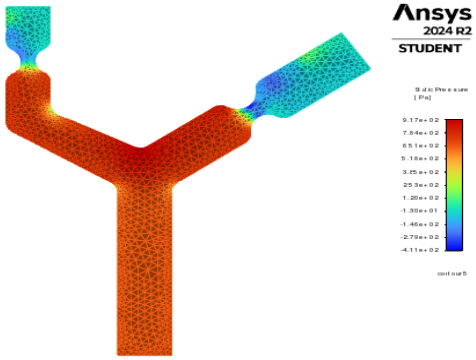

(A) Contour representation of static pressure.

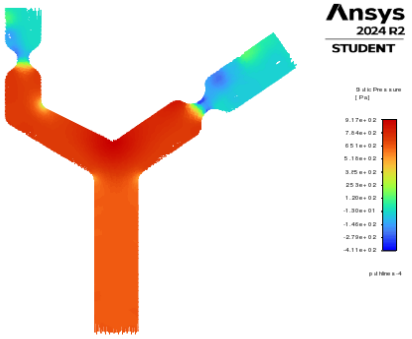

(B) Pathlines representation of static pressure.

FIGURE 11. Contour and pathlines graphs for static pressure of carotid stenosis artery.

In the Figure 12, as blood passes through the stenosed carotid artery, the dynamic pressure contours and pathlines show notable changes. Because of the constant and mostly undisturbed velocity of blood entering the artery, the dynamic pressure at the entrance is quite high, measuring $2.24 \times 10^2 Pa$ (light blue). The dynamic pressure lowers dramatically to $0.84 \times 10^{-2} Pa$ (dark blue) when blood gets closer to the stenosis. Blood velocity starts to rise as a result of the narrowing artery's initial energy redistribution, although dynamic pressure is momentarily repressed because of the transition phase of flow acceleration. When the blood velocity reaches its maximum within the stenosis, the dynamic pressure peaks at $1.12 \times 10^3 Pa$ (red). According to Bernoulli's principle, the blood accelerates due to the extreme constriction, changing static pressure into dynamic pressure. Dynamic

pressure drops along the arterial walls once again after leaving the stenosis, but it stays greater in the artery's center. This pattern occurs because the core flow maintains left-over kinetic energy from the stenosed zone, while the greater cross-section slows the blood near the walls owing to friction and turbulence. These changes demonstrate the hemodynamic effects of stenosis, since pressure variations throughout the artery are influenced by velocity-driven energy redistribution.

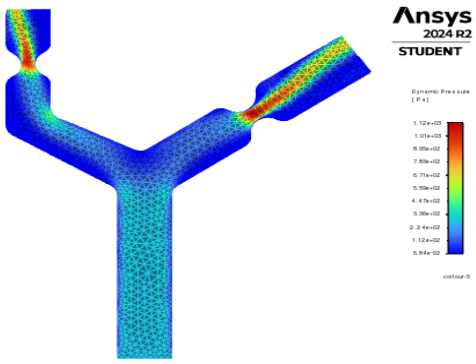

(A) Contour representation of dynamic pressure.

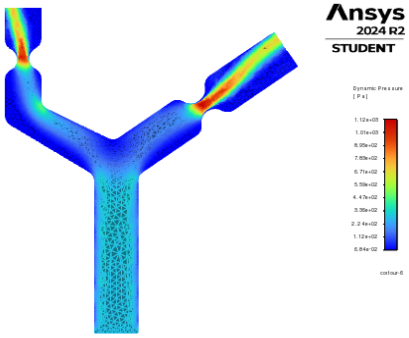

(B) Pathlines representation of dynamic pressure.

FIGURE 12. Contour and pathlines graphs for dynamic pressure of carotid stenosis artery.

In the Figure 13, as blood flows via the carotid artery, the velocity magnitude contours and pathlines show unique flow features, particularly when stenosis is present. The velocity near the artery walls at the intake is $1.50 \times 10^{-1} m/s$, which is relatively low and is indicated in blue. Due to friction between the blood and the walls, the velocity decreases close to the borders, creating a velocity profile where the flow is quickest in the middle and slowest at the walls. Conversely, the center section of the artery, which is indicated by yellow and has a velocity of $8.98 \times 10^{-1} m/s$, has a faster velocity and less frictional resistance, allowing blood to flow more easily. The velocity increases sharply as the flow

passes through the stenosis and approaches it, peaking at $1.50 \times 10^0 m/s$ (red). This dramatic increase in velocity happens as a result of the artery constriction, which raises the flow speed to preserve mass conservation by forcing the same amount of blood through a smaller cross-sectional area. The fact that there is less room for the flow is the immediate cause of this acceleration, which is in line with the continuity equation's prediction that velocity increases as cross-sectional area decreases. Because of the acceleration of blood in the stenosed zone, stenosis can drastically modify blood flow dynamics, as evidenced by the observed variations in velocity magnitude.

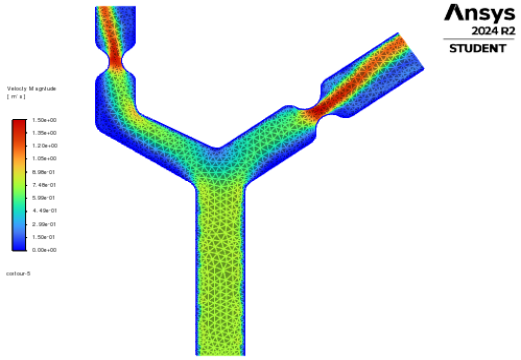

(A) Contour representation of velocity magnitude.

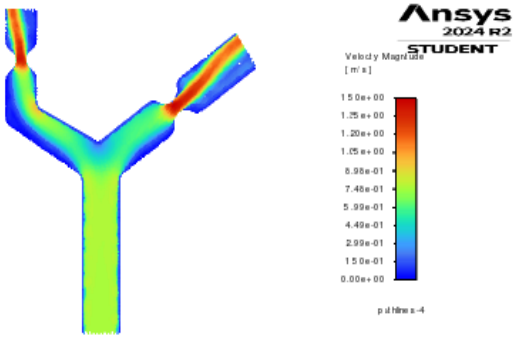

(B) Pathlines representation of velocity magnitude.

FIGURE 13. Contour and pathlines graphs for velocity magnitude of carotid stenosis artery.

6.1. **Model velocity Validation.** In order to verify the effectiveness of the model in use, In reference[60], the model constructed has been evaluated with the velocity profile of cases, non-pathological flow in cylindrical arteries, pathological flow in cylindrical arteries, and non-pathological flow in 2D bifurcated arteries. Table 8 shows that non-pathological flow in the cylindrical artery case showed almost the same fluctuation in the velocity profile

values of the two models, whereas other cases showed convergence. About the confirmation of cases of "normal/stenosed carotid artery" and "stenosed bifurcated artery," A professional medical committee from Nile Scan's cardiovascular section in Egypt carried out the certification. There are three doctors on the group with over 15 years of cardiovascular experience. Our model and MRI were used by the committee to diagnose "the normal/stenosed carotid artery" and "the stenosed bifurcated artery," and the results were equal in both cases. The simulation results are validated on two fronts:

TABLE 8. Model Validation

Case Name	**Velocity in m/s in our research**	**Velocity in m/s for reference model** [60]
Non-pathological flow in cylindrical artery	0.28	0.26
Pathological flow in the cylindrical artery	0.22	0.35
Non-pathological flow in 2D bifurcated artery	0.48	0.39

(1) Quantitative validation against a reference model [60] showed good agreement in velocity values, particularly for non-pathological cylindrical artery cases (0.28 m/s in our model vs. 0.26 m/s in reference).
(2) Clinical validation is conducted by a medical committee at Nile Scan, Egypt, who analyzed MRI-based diagnosis of stenosis in patient-specific models and confirmed that the simulation outputs matched clinical interpretations. This dual-validation approach strengthens confidence in the model's applicability to real-world diagnostic and treatment scenarios.
In the Figure 14, the carotid artery's flow distribution is clearly seen through the streamlines and stream function contours. At $1.70 \times 10^2 m^2/s$, the blue hue indicates a low stream function value on the right side of the artery, close to the wall. Because of the no-slip situation at the boundary, blood moves more slowly in this area, which is reflected in the lower stream function close to the wall. The blood encounters frictional resistance as it contacts the artery wall, which lowers the flow velocity close to the border and, ultimately, the stream function value. On the other hand, the stream function value on the left side of the artery is greater, as indicated by the red value of $8.82 \times 10^2 m^2/s$. Because there is less frictional resistance here than on the right, the higher value translates into a higher flow rate and velocity. Because there isn't a substantial wall border on the left side, blood may flow more freely, increasing circulation and stream function. The no-slip condition at the walls and the ensuing variations in flow velocity directly cause the variation in stream function across the artery.
In the Figure 15, the pathlines and contours of the static temperature provide crucial information on the thermal behavior of the blood flow in the carotid artery. With a value of $3.24 \times 10^2 K$, the static temperature is higher along the artery walls and is shown as light green. Because of the frictional forces between the blood and the artery walls, which produce heat through viscous dissipation, the temperature near the walls rises. There is a buildup of thermal energy in the areas close to the walls because the slower blood circulation (caused by the no-slip condition) means that less heat is removed by the fluid. The static temperature near the artery's middle, which is shown in blue and has a value of $3.00 \times 10^2 K$, is lower. The quicker blood flow in the central region, which improves convective heat transfer and makes it possible for heat to be efficiently transported away

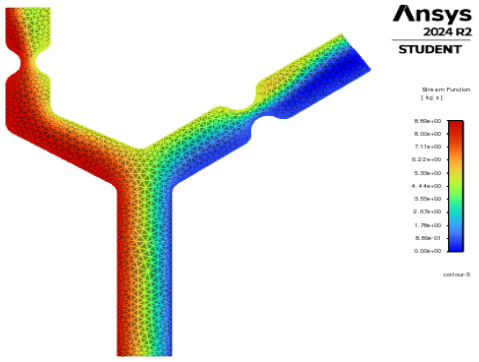

(A) Contour representation of stream function.

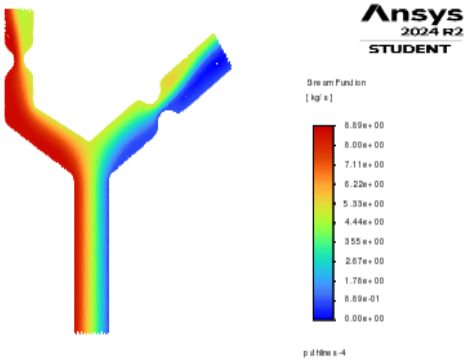

(B) Pathlines representation of stream function.

FIGURE 14. Contour and pathlines graphs for stream function of carotid stenosis artery.

from the artery core, is the cause of this drop in temperature. Less heat is absorbed in the core section as blood flows through it more quickly. The temperature of a material (in this example, blood) in relation to its environment is known as its static temperature, and it is affected by the blood's flow properties as well as the frictional interactions with the arterial walls. A direct result is the temperature gradient that is seen.

In the Figure 16, the thermal behavior of blood as it travels through the carotid artery, especially as it goes through the stenosed zone, is clearly depicted by the total temperature contours and pathlines. The blood enters the inlet with a pale green color and a modest overall temperature of $3.00 \times 10^{+02} K$. Due to the blood's initially steady temperature, this value remains constant throughout the artery. The artery's overall temperature stays mild, suggesting a constant flow with even heat distribution and little thermal disturbance from friction or the wall. However, the overall temperature noticeably changes as the blood flows through the stenosis. The overall temperature close to the artery walls drops dramatically after stenosis, reaching $3.00 \times 10^{-02} K$, as seen in blue. Convective heat transfer is

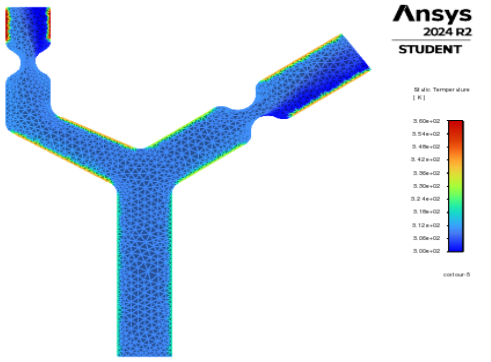

(A) Contour representation of static temperature.

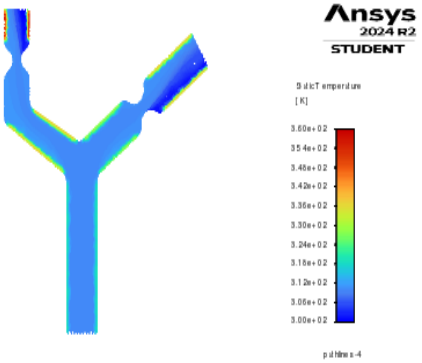

(B) Pathlines representation of static temperature.

FIGURE 15. Contour and pathlines graphs for static temperature of carotid stenosis artery.

improved by the faster blood flow through the constricted portion of the artery, which results in this decrease in overall temperature. The stenosis's high blood flow velocity results in a more effective transfer of thermal energy away from the walls, lowering the ambient temperature in those areas. The stark difference between the overall temperature before and after stenosis emphasizes how flow acceleration affects heat distribution, causing the temperature near the wall to drop significantly as blood passes through.

6.2. **Line graphs of static pressure along walls, inlet, outlet and stenosis portions for carotid stenosis artery.** In the Figure 17 (a), the line graph shows how the static pressure varies between the outlets, stenosis, and intake. The maximum static pressure, shown by aqua blue and recorded at $6.00 \times 10^{02} Pa$, lies near the intake. Because of flow restriction, the pressure rises to the same value $(6.00 \times 10^{02} Pa)$ at stenosis levels 1 and 2, as indicated by the orange and blue lines. However, as seen by the red and purple hues, the static pressure drastically decreases to $1.00 \times 10^{02} Pa$ at both exits (1 and 2). As the blood leaves

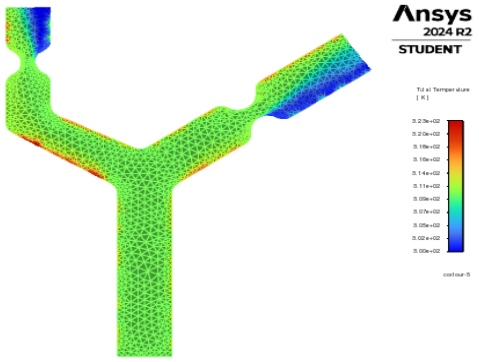

(A) Contour representation of total temperature.

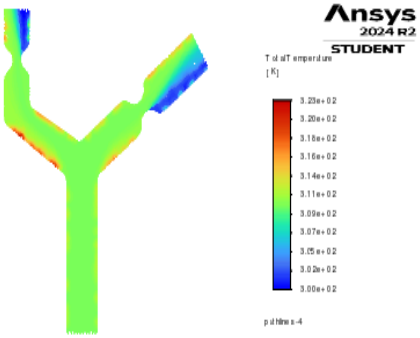

(B) Pathlines representation of total temperature.

FIGURE 16. Contour and pathlines graphs for static temperature of carotid stenosis artery.

the artery, energy dissipation is reflected in this drop at the outputs. The graph does a good analysis of illustrating how stenosis and outlet conditions affect pressure dynamics.

In the Figure 17 (b), the distribution of static pressure along the five artery walls is seen in the line graph. The static pressure is $6.00 \times 10^2 Pa$ at Wall 1 and rises to $7.00 \times 10^2 Pa$ at Wall 2, which is on the right. The red line for wall 3 shows the dramatic reduction in static pressure to $-2.00 \times 10^2 Pa$ after the blood has passed through the stenosis. The pressure on the left side increases to $6.50 \times 10^2 Pa$ prior reaching the stenosis at wall 4, but after going through it, it drastically drops to $-2.00 \times 10^{-2} Pa$ at wall 5. This variant emphasizes how flow dynamics and constriction alter pressure.

6.3. **Line graphs of dynamic pressure along walls, inlet, outlet and stenosis portions for carotid stenosis artery.** In the Figure 18 (a), dynamic pressure changes at the inlet, outlets, and stenosis levels are shown in the line graph. The dynamic pressure begins at

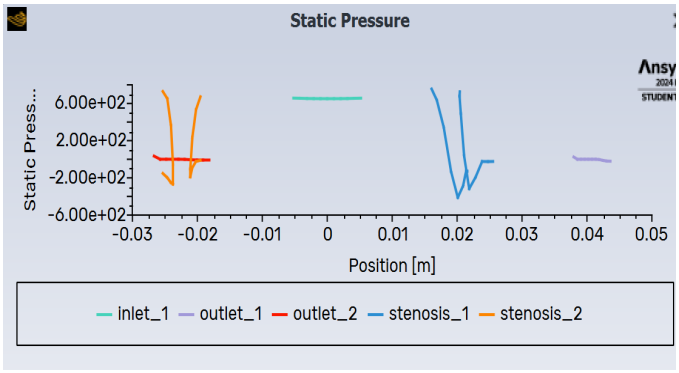

(A) Static pressure at inlet, outlet and stenosis areas.

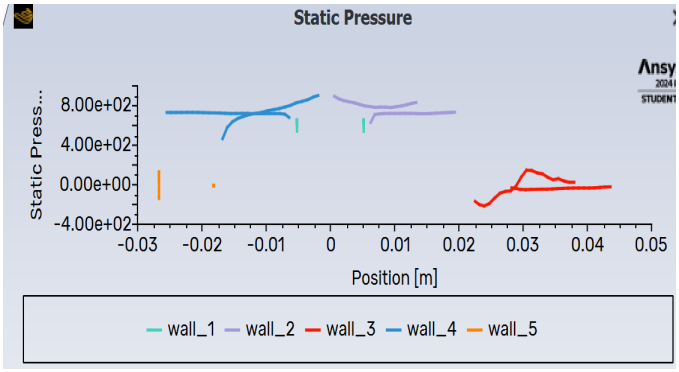

(B) Static pressure along different walls of carotid artery.

FIGURE 17. Line graphs of static pressure through carotid stenosis artery.

$2.00 \times 10^2 Pa$ at the intake. The pressure rises dramatically at both exits (1 and 2), from -0.02 to -0.03 Pa to a high of $7.00 \times 10^2 Pa$. The dynamic pressure increases to $4.00 \times 10^2 Pa$ for stenosis levels 1 and 2, indicating the impact of flow acceleration brought on by constriction. These changes show how stenosis and flow velocity affect the distribution of pressure.

In the Figure 18 (b), the dynamic pressure distribution across the five artery walls is displayed on the line graph. The dynamic pressure rises to $2.50 \times 10^2 Pa$ at Wall 1, next to the inlet, and falls to $0.50 \times 10^2 Pa$ at Wall 2, on the right. Once the dynamic pressure has passed through the stenosis, it increases to $3.00 \times 10^2 Pa$. The dynamic pressure stays at $2.50 \times 10^2 Pa$ on the left side (Wall 4), prior to the stenosis, and at Wall 5, suggesting localized changes impacted by stenosis and flow dynamics.

6.4. **Line graphs of velocity and surface Nusselt number along inlet, outlet and stenosis portions for carotid stenosis artery.** In the Figure 20 (a), the blood flow velocity

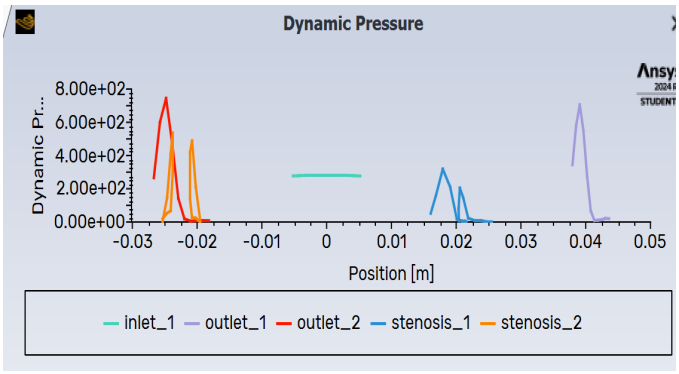

(A) Dynamic pressure at inlet, outlet and stenosis areas.

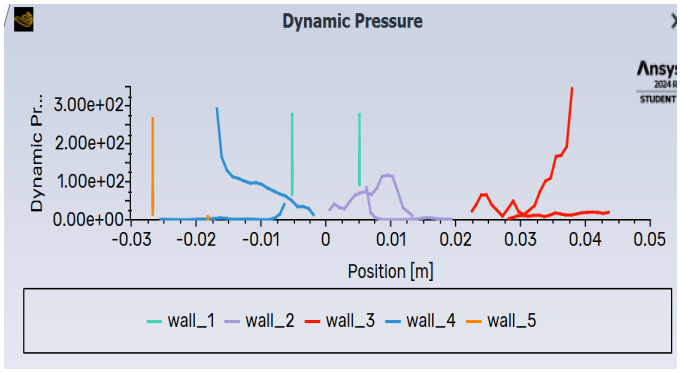

(B) Dynamic pressure along different walls of carotid artery.

FIGURE 18. Line graphs of dynamic pressure through carotid stenosis artery.

fluctuations from the entrance to the stenosis and beyond are depicted in the line graph. The velocity at the entrance is $4.00 \times 10^{-02} m/s$, which is typical. Because to flow limitation, the blood's velocity drops to $2.00 \times 10^{-01} m/s$ when it passes between Stenosis 1 and 2. The velocity, however, dramatically jumps to $1.20 \times 10^{oo} m/s$ after passing through the stenosis, indicating the acceleration brought on by downstream recovery and decreased cross-sectional area.

In the Figure 20 (b), the surface Nusselt number fluctuations over the inlet, outlets, and stenosis levels are depicted in the line graph. With a value of 5.00×10^2, the surface Nusselt number at the intake is comparatively modest, suggesting moderate heat transmission. The surface Nusselt number further drops to insignificant levels at outlets 1 and 2. The surface Nusselt number, however, dramatically rises to 2.50×10^3 at stenosis 1 and 2, indicating improved heat transfer as a result of the stenosis zones' higher fluid velocity and turbulence.

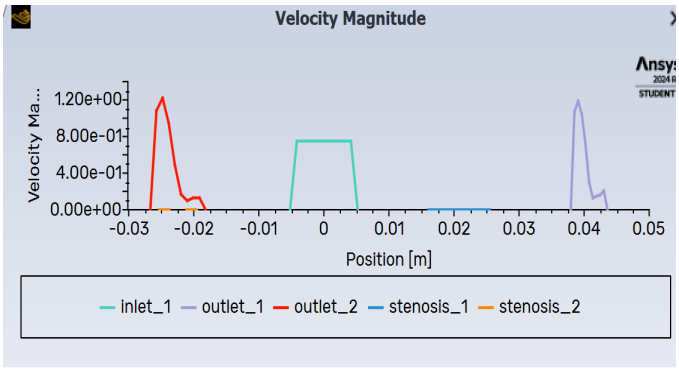

(A) Velocity magnitude at inlet, outlet and stenosis areas.

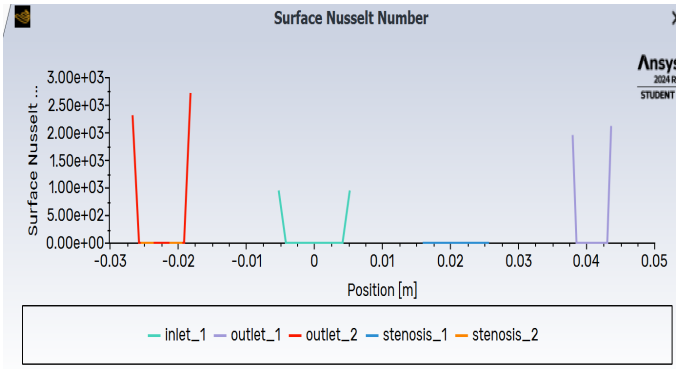

(B) Surface nusslet number at inlet, outlet and stenosis areas.

FIGURE 19. Line graphs of velocity magnitude and surface nusslet number through carotid stenosis artery.

6.5. **Line graphs of static temperature along walls, inlet, outlet and stenosis portions for carotid stenosis artery.** In the Figure **??** (a), with a value of $3.10 \times 10^{02} K$, the static temperature distribution displays lower values in the entrance and outflow areas, where heat production is negligible. However, the velocity rises as the blood passes through the stenosis, increasing heat production and friction. As a result, the static temperature at the stenosis area rises, reaching a measured $3.20 \times 10^{02} K$. The increased thermal effects brought on by the limited flow and turbulence in these regions are reflected in the stenosis's higher static temperature.

In the Figure **??**(b), as blood passes through the artery, there is an increasing tendency in the static temperature distribution along the walls. The static temperature at Wall 1, next to the entrance, is comparatively low at $3.17 \times 10^{02} K$. The temperature rises somewhat to $3.27 \times 10^{02} K$ at Wall 2 and then to $3.35 \times 10^{02} K$ at Wall 3, as shown by the red line. The static temperature is $3.37 \times 10^{02} K$ prior to the stenosis at Wall 4, but it increases to a high of $3.55 \times 10^{02} K$ following passage through the stenosis, representing the heat produced by turbulence and flow restriction.

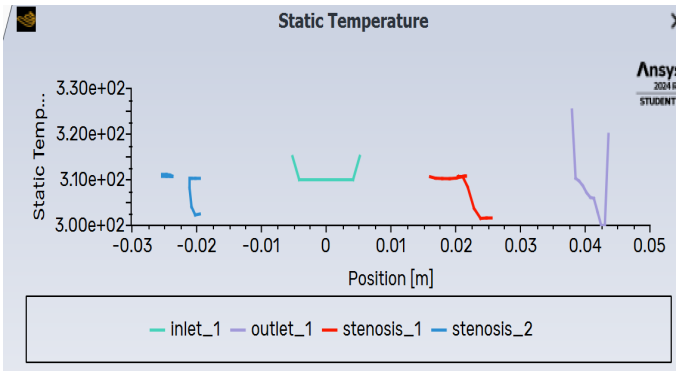

(A) Static temperature at inlet, outlet and stenosis areas.

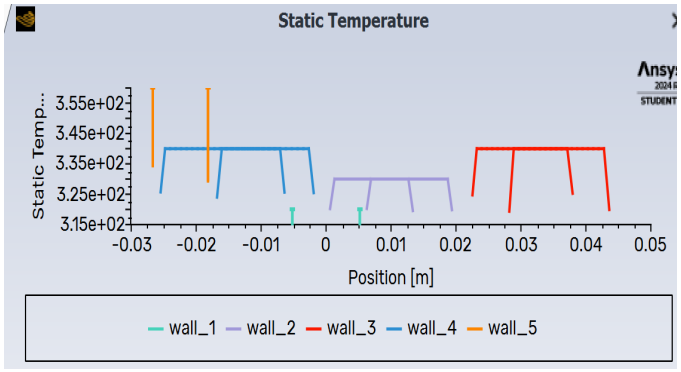

(B) Static temperature along different walls of carotid artery.

FIGURE 20. Line graphs of static pressure through carotid stenosis artery.

6.6. **Influence of Temperature on Hemodynamic Parameters.** The inclusion of temperature in the governing equations affected velocity and pressure distributions via thermally-induced viscosity changes. Increased friction near arterial walls led to localized heating as shown in Figure 15, which slightly reduced viscosity, flattening the velocity profile is shown in Figure 13 and allowing smoother post-stenosis flow. Consequently, minor variations in pressure recovery patterns are shown in Figure 11 were observed. These effects, though quantitatively modest, are relevant for studying heat-based treatment methods and energy loss mechanisms in diseased arteries.

6.7. **Reynolds Number and Flow Regime Justification.** The Reynolds number was calculated using characteristic artery diameter and peak systolic velocity, yielding $Re \approx 909$, which confirms the predominance of laminar flow under physiological conditions. However, localized flow acceleration in stenosed regions could induce transitional behavior. Though a laminar flow model was used here, future investigations may consider low-Re turbulence models to capture transient vortical effects more accurately.

6.8. **Advantages of the Obtained Solutions.** The obtained solutions offer several key advantages:

- **Realistic Hemodynamic Prediction:** The use of the Casson fluid model and finite volume method provides accurate velocity, pressure, temperature, and WSS distributions in stenosed carotid arteries under realistic physiological conditions.
- **Better Clinical Insight:** The solutions help in understanding critical flow alterations such as high wall shear stress zones and pressure drops, which are associated with plaque rupture and stroke risk.
- **Mesh Independence Validated:** The mesh refinement study ensures that the results are reliable, independent of grid resolution, and computationally efficient.
- **Temperature Effects Analyzed:** Including temperature distribution adds an important thermal aspect to blood flow studies, which is useful for heat-based treatments like hyperthermia.
- **Foundation for Patient-Specific Modeling:** The methodology can be easily extended to 3D and patient-specific geometries using MRI or CT data for personalized diagnostic and therapeutic planning.

TABLE 9. List of Notations

Symbol	Description	Unit
C_f	Skin friction coefficient	–
D	Diameter of cylinder	m
E	Young's modulus	Pa
F_D	Drag force	N
G	Shear modulus	Pa
H	Height of the cylinder	m
L	Length of the cylinder or characteristic length	m
M	Mass of the structure	kg
Re	Reynolds number	–
St	Strouhal number	–
U	Free-stream velocity	m/s
V	Velocity	m/s
Y	Displacement in transverse direction	m
α	Angle of attack	degree
μ	Dynamic viscosity	Pa·s
ν	Kinematic viscosity	m^2/s
ρ	Fluid density	kg/m^3
σ	Stress	Pa
θ	Angular displacement	rad

The notations that is used in article are given in Table 9.

6.9. **Physical Applications of Study.** The present study provides valuable insights into the effects of stenosis severity and Reynolds number on hemodynamic parameters such as pressure drop, velocity profiles, and wall shear stress (WSS) in blood flow through

stenosed arteries. These findings have direct implications for cardiovascular diagnostics and medical device design. From a clinical standpoint, understanding the nonlinear relationship between pressure drop and both Reynolds number and stenosis severity is crucial. This relationship can guide cardiologists in interpreting pressure gradients obtained from catheter-based measurements like fractional flow reserve (FFR). For instance, the observed sharp increase in pressure drop at high stenosis severities supports the rationale behind revascularization decisions for lesions causing critical narrowing. Moreover, the detailed velocity field and shear stress distribution provide insights into conditions favorable to atherosclerotic plaque rupture or thrombus formation. High WSS and disturbed flow regions, which become more pronounced at severe stenosis and elevated Reynolds numbers, are linked to endothelial dysfunction and intimal damage—factors contributing to plaque destabilization. These findings may inform the design and placement of stents and other vascular implants, ensuring they minimize hemodynamic disturbances that could exacerbate disease progression. From a biomechanical engineering perspective, the numerical simulations validate key assumptions used in the design of cardiovascular devices. For instance, pressure recovery downstream of stenosis is a critical consideration in prosthetic valve and stent development. The results also offer valuable boundary condition parameters for larger-scale or patient-specific simulations used in computational hemodynamics. In future applications, the computational methodology adopted in this study could be extended to model pulsatile flow, non-Newtonian fluid properties of blood, or patient-specific geometries derived from medical imaging. These extensions would further bridge the gap between theoretical analysis and clinical relevance, enabling personalized diagnostics and treatment planning.

7. CONCLUSION

This study highlights the significant impact of fluid dynamics on the structural properties of descending arteries, particularly focusing on the carotid artery's geometry. It emphasizes that idealized geometric models of the carotid artery can lead to errors in predicting local features critical for diagnosing diseases, as they overlook the complexities present in actual arterial shapes. The study demonstrates that arterial geometries with curvatures, bends, and tapering significantly affect blood flow behavior, leading to variations in velocity, pressure, and wall shear stress (WSS). It was observed that velocity profiles differ between 2D and 3D geometries, with higher velocities occurring during systole and non-uniform flow distributions due to irregularities in arterial surfaces. The comparison underscores the importance of using accurate, real-world geometrical data, obtained from methods like CT or MRI scans, to predict more precise regional flow characteristics. This research suggests that future studies should focus on refining imaging techniques and adopting more accurate models for better disease diagnosis and treatment planning.

In future studies, machine learning techniques could be integrated with CFD simulations to develop surrogate models for rapid prediction, extract features from imaging data, and optimize treatment strategies. This hybrid approach has the potential to significantly reduce computational time while maintaining high predictive accuracy, paving the way for real-time diagnostic tools and personalized medicine in vascular disease modeling.

Acknowledgments: All the authors are obliged and thankful to the University of Management and Technology, Lahore, Pakistan, for facilitating and supporting the research work.

Author's Contributions: Writing-original draft preparation, Formal analysis, Problem formulation: A.W and S.K; Investigation, Methodology, Supervision, Resources, Validation: M.I.A, A.W and K.A; Graphical discussion, Software, Review and editing: A.W and K.A. All authors have read and agreed to the published version of the manuscript.

Funding:
This research received no external funding.

Data Availability: Data sharing is not applicable to this article as no data sets were generated or analyzed during the current study.

Conflicts of interest: The authors declare that they have no conflicts of interest.

REFERENCES

[1] M. A. Abazari, D. Rafiei, M. Soltani, & M. Alimohammadi, The effect of beta-blockers on hemodynamic parameters in patient-specific blood flow simulations of type-B aortic dissection: A virtual study, Scientific reports, **11**, No. 1 (2021) 16058.

[2] K. Andelovic, P. Winter, P. M. Jakob, W. R. Bauer, V. Herold, & A. Zernecke, Evaluation of plaque charac-teristics and inflammation using magnetic resonance imaging, Biomedicines, **9**, No. 2 (2021) 185.

[3] H. Attar, T. Ahmed, R. Rabie, A. Amer, M. R. Khosravi, A. Solyman, & M. A. Deif, Modeling and com-putational fluid dynamics simulation of blood flow behavior based on MRI and CT for Atherosclerosis in Carotid Artery, Multimedia Tools and Applications, **83**, No. 19 (2024) 56369-56390.

[4] R. M. Attia, & M. A. Eldosoky, Studying of the blood flow behavior in a stenosed carotid artery for healthy, anemic and diabetic blood, IEEE, **121**, No. 2 (2020) 72-75.

[5] A. Bajraktari, I. Bytyci, & M. Y. Henein, High coronary wall shear stress worsens plaque vulnerability: a systematic review and meta-analysis, Angiology, 72, No. 8 (2021) 706-714.

[6] L. F. Buckley, & P. Libby, Colchicine's Role in Cardiovascular Disease Management, Arteriosclerosis, Thrombosis, and Vascular Biology, **44**, No. 3 (2024) 1031-1041.

[7] V. Carvalho, N. Rodrigues, R. Ribeiro, P. F. Costa, J. C. Teixeira, R. A. Lima, & S. F. Teixeira, Hemody-namic study in 3D printed stenotic coronary artery models: Experimental validation and transient simulation, Computer methods in biomechanics and biomedical engineering, **24**, No. 6 (2021) 623-636.

[8] T. Chakraborty, Z. S. Venter, Y. Qian, & X. Lee, Lower urban humidity moderates outdoor heat stress, Agu Advances, 3, No. 5 (2022) e2022AV000729.

[9] C. X. Chen, Y. Ding, & J. A. Gear, Numerical simulation of atherosclerotic plaque growth using two-way fluid–structural interaction, The ANZIAM Journal, **53**, No. 4 (2012) 278-291.

[10] Y. Chen, J. Liu, M. Li, Y. Yu, Z. Yan, W. Shiu, ... & W. Xu, Non-invasive assessment of intracranial wall shear stress using high-resolution magnetic resonance imaging in combination with computational fluid dynamics technique, Fundamental Research, **2**, No. 2 (2022) 329-334.

[11] T. A. Chowdhury, & P. Das, Computational Study and Analysis of Carotid Artery Stenosis, Journal of Engineering Advancements, **5**, No. 2 (2024) 35-50.

[12] A. Darvesh, M. Sánchez-Chero, C. A. Reyes Reyes, P. A. S. Céspedes, M. T. Alvarez, M. F. U. Cárdenas, & C. E. Rosas-Prado, Mathematical analysis of bio-nanofluid flow over a nonlinear tapering artery with stenosis conditions using cross fluid viscosity model, BioNanoScience, **13**, No. 4 (2023) 2082-2095.

[13] H. Do, A. A. Owida, W. Yang, & Y. S. Morsi, Numerical simulation of the haemodynamics in end-to-side anastomoses, International Journal for Numerical Methods in Fluids, 67, No. 5 (2011) 638-650.

[15] A. Elhanafy, A. Elsaid, & A. Guaily, Numerical investigation of hematocrit variation effect on blood flow in an arterial segment with variable stenosis degree, Journal of Molecular Liquids, 313, (2020) 113550.

[16] R. El Sayed, C. C. Park, Z. Shah, F. B. Nahab, D. C. Haussen, J. W. Allen, & J. N. Oshinski, Assessment of complex flow patterns in patients with carotid webs, patients with carotid atherosclerosis, and healthy subjects using 4D flow MRI, Journal of Magnetic Resonance Imaging, **59**, No. 6 (2024) 2001-2010.

[17] G. Fatima, & A. A. Khan, Stratified Hydromagnetic Gas-Liquid Flow in a Wavy Channel, Punjab Univ. J. Math., 56, No. 6 2024.

[18] M. A. Fernandez, L. Formaggia, J. F. Gerbeau, & A. Quarteroni, Modeling and simulation of the circulatory system, MS&A–Modeling, Simulation and Applications, Cardiovascular Mathematics, **1**, No. 3 (2009).

[19] P. T. Gamage, P. Dong, J. Lee, Y. Gharaibeh, V. N. Zimin, L. A. Dallan, ... & L. Gu, Hemodynamic alternations following stent deployment and post-dilation in a heavily calcified coronary artery: In silico and ex-vivo approaches, Computers in biology and medicine, **139**, (2021) 104962.

[20] R. L. Hewlin, & J. P. Kizito, Development of an experimental and digital cardiovascular arterial model for transient hemodynamic and postural change studies:"A preliminary framework analysis", Cardiovascular Engineering and Technology, **9**, (2018) 1-31.

[21] S. S. Hossain, Z. Starosolski, T. Sanders, M. J. Johnson, M. C. Wu, M. C. Hsu, ... & A. Annapragada, Image-based patient-specific flow simulations are consistent with stroke in pediatric cerebrovascular disease, Biomechanics and modeling in mechanobiology, **20**, (2021) 2071-2084.

[22] M. Jawad, K. Shehzad, & R. Safdar, Novel computational study on MHD flow of nanofluid flow with gyrotactic microorganism due to porous stretching sheet, Punjab University Journal of Mathematics, **52**, No. 12 (2021).

[23] F. Kabinejadian, D. N. Ghista, B. Su, M. K. Nezhadian, L. P. Chua, J. H. Yeo, & H. L. Leo, In vitro measurements of velocity and wall shear stress in a novel sequential anastomotic graft design model under pulsatile flow conditions, Medical Engineering & Physics, 36, No. 10 (2014) 1233-1245.

[24] A. Karimi, M. Navidbakhsh, A. Shojaei, & S. Faghihi, Measurement of the uniaxial mechanical properties of healthy and atherosclerotic human coronary arteries, Materials Science and Engineering: C, 33, No. 5 (2013) 2550-2554.

[25] S. Kamangar, I. A. Badruddin, N. Ameer Ahamad, M. E. M. Soudagar, K. Govindaraju, N. Nik-Ghazali, ... & T. M. Yunus Khan, Patient specific 3-d modeling of blood flow in a multi-stenosed left coronary artery, Biomedical materials and engineering, 28, No. 3 (2017) 257-266.

[26] V. Kashyap, B. B. Arora, & S. Bhattacharjee, A computational study of branch-wise curvature in idealized coronary artery bifurcations, Applications in Engineering Science, **4**, (2020) 100027.

[27] A. S. Khan, A. Shahzad, M. Zubair, A. Alvi, & R. Gul, Personalized 0D models of normal and stenosed carotid arteries, Computer methods and programs in biomedicine, 200, (2021) 105888.

[28] D. N. Ku, Blood flow in arteries, Annual review of fluid mechanics, **29**, No. 1 (1997) 399-434.

[29] J. F. LaDisa, L. E. Olson, H. A. Douglas, D. C. Warltier, J. R. Kersten, & P. S. Pagel, Alterations in re-gional vascular geometry produced by theoretical stent implantation influence distributions of wall shear stress: analysis of a curved coronary artery using 3D computational fluid dynamics modeling, Biomedical engineering online, 5, (2006) 1-11.

[30] B. B. Lieber, M. Siebes, & T. Yamaguchi, Correlation of hemodynamic events with clinical and pathological observations, Annals of biomedical engineering, 33, (2005) 1695-1703.

[31] D. Lopes, H. Puga, J. Teixeira, & R. Lima, Blood flow simulations in patient-specific geometries of the carotid artery: A systematic review, Journal of Biomechanics, **111**, (2020) 110019.

[32] K. Masdjedi, L. J. van Zandvoort, M. M. Balbi, F. J. Gijsen, J. M. Ligthart, M. C. Rutten, ... & J. Daemen, Validation of a three-dimensional quantitative coronary angiography-based software to calculate fractional flow reserve: the FAST study, EuroIntervention, 16, No. 7 (2020) 591-599.

[33] S. Mukhopadhyay, P. R. De, K. Bhattacharyya, & G. C. Layek, Casson fluid flow over an unsteady stretching surface, Ain Shams Engineering Journal, **4**, No. 4 (2013) 933-938.

[34] S. S. Mulani, & P. I. Jagad, Analysis of the effects of plaque deposits on the blood flow through human artery, Int. Eng. Res. J, **41**, No. 2 (2015) 2319-3182.

[35] G. Nannini, A. Caimi, M. C. Palumbo, S. Saitta, L. N. Girardi, M. Gaudino, ... & A. Redaelli, Aortic hemodynamics assessment prior and after valve sparing reconstruction: A patient-specific 4D flow-based FSI model, Computers in Biology and Medicine, 135, (2021) 104581.

[36] M. Nardin, M. Verdoia, D. Cao, S. Nardin, E. Kedhi, G. Galasso, ... & G. De Luca, Platelets and the atherosclerotic process: an overview of new markers of platelet activation and reactivity, and their implications in primary and secondary prevention, Journal of Clinical Medicine, 12, No. 18 (2023) 6074.

[37] A. Nooraeen, H. Taghizadeh, & F. Ghalichi, Hemodynamic coupling between a primary atherosclerotic plaque and subsequent secondary lesions, Physics of Fluids, **36**, No. 6 (2024).

[38] A. Pandey, M. S. Khan, K. V. Patel, D. L. Bhatt, & S. Verma, Predicting and preventing heart failure in type 2 diabetes, The Lancet Diabetes & Endocrinology, 11, No. 8 (2023) 607-624.

[39] R. Pandey, M. Kumar, J. Majdoubi, M. Rahimi-Gorji, & V. K. Srivastav, A review study on blood in human coronary artery: Numerical approach, Computer methods and programs in biomedicine, 187, (2020) 105243.

[40] P. Parissis, A. Romeos, A. Giannadakis, A. Kalarakis, & M. Peroulis, Computational Study of Hemodynamic Field of an Occluded Artery Model with Anastomosis, Bioengineering 2023, 10, (2023) 146.

[41] A. V. Poznyak, L. V. Nedosugova, V. N. Sukhorukov, A. A. Melnichenko, E. M. Pleshko, & A. N. Orekhov, Hepatitis C and atherosclerosis: inflammatory interplay, Journal of Angiotherpay, **7**, No. 1 (2023) 1-10.

[42] A. Razavi, E. Shirani, & M. R. Sadeghi, Numerical simulation of blood pulsatile flow in a stenosed carotid artery using different rheological models, Journal of biomechanics, 44, No. 11 (2011) 2021-2030.

[43] R. O. Rodrigues, P. C. Sousa, J. Gaspar, M. Bañobre-López, R. Lima, & G. Minas, Organ-on-a-chip: A preclinical microfluidic platform for the progress of nanomedicine, Small, **16**, No. 51 (2020) 2003517.

[44] H. Samady, P. Eshtehardi, M. C. McDaniel, J. Suo, S. S. Dhawan, C. Maynard, ... & D. P. Giddens, Coronary artery wall shear stress is associated with progression and transformation of atherosclerotic plaque and arterial remodeling in patients with coronary artery disease, Circulation, 124, No. 7 (2011) 779-788.

[45] W. P. Santamore, P. Walinsky, A. A. Bove, R. H. Cox, R. A. Carey, & J. F. Spann, The effects of vasocon-striction on experimental coronary artery stenosis, American Heart Journal, **100**, No. 6 (1980) 852-858.

[46] F. Settecase, & V. L. Rayz, Advanced vascular imaging techniques, Handbook of Clinical Neurology, 176, (2021) 81-105.

[47] K. A. Smith, S. S. Merchant, E. W. Hsu, & L. H. Timmins, Effect of subject-specific, spatially reduced, and idealized boundary conditions on the predicted hemodynamic environment in the murine Aorta, Annals of Biomedical Engineering, 49, (2021) 3255-3266.

[48] P. Soni, S. Kumar, B. R. Kumar, S. K. Rai, A. Verma, & O. Shankar, A comprehensive review on CFD simulations of left ventricle hemodynamics: numerical methods, experimental validation techniques, and emerging trends, Journal of the Brazilian Society of Mechanical Sciences and Engineering, 46, No. 5 (2024) 301.

[49] S. Sriyab, Mathematical Analysis of Non-Newtonian Blood Flow in Stenosis Narrow Arteries, Computational and mathematical methods in medicine, **2014**, No. 1 (2014) 479152.

[50] I. O. Starodumov, S. Y. Sokolov, D. V. Alexandrov, A. Y. Zubarev, I. S. Bessonov, V. V. Chestukhin, & F. A. Blyakhman, Modelling of hemodynamics in bifurcation lesions of coronary arteries before and after myocardial revascularization, Philosophical Transactions of the Royal Society A, **380**, No. 2217 (2022) 20200303.

[51] M. Tomaszewski, K. Sybilski, P. Baranowski, & J. Malachowski, Experimental and numerical flow analysis through arteries with stent using particle image velocimetry and computational fluid dynamics method, Biocybernetics and Biomedical Engineering, **40**, No. 2 (2020) 740-751.

[52] E. Tóth, M. Fagyas, B. Nagy Jr, I. M. Siket, B. Szőke, L. Mártha, ... & A. Tóth, Distinct subsets of anti-pulmonary autoantibodies correlate with disease severity and survival in severe COVID-19 patients, GeroScience, **46**, No. 2 (2024) 1561-1574.

[53] N. Uemiya, C. J. Lee, S. Ishihara, F. Yamane, Y. Zhang, & Y. Qian, Analysis of restenosis after carotid artery stenting: preliminary results using computational fluid dynamics based on three-dimensional angiography, Journal of Clinical Neuroscience, **20**, No. 11 (2013) 1582-1587.

[54] A. Wahab, M. I. Asjad, M. B. Riaz, & J. A. Haider, Modeling and simulation of blood flow in unhealthy elliptic arteries with computational fluid dynamics approach, PloS one, **20**, No. 4 (2025) e0317989.

[55] S. A. Wajihah, & D. S. Sankar, A review on non-Newtonian fluid models for multi-layered blood rheology in constricted arteries, Archive of Applied Mechanics, **93**, No. 5 (2023) 1771-1796.

[56] A. Warey, J. Gao, & R. O. Grover Jr, Generalization performance of a deep learning based engine-out emissions model, Energy and AI, **5**, (2021) 100080.

[57] T. Xiaoyong, C. Yuping, H. Wei, C. Juan, Q. Feng, & L. Zhuo, Evaluation of the efficacy of Wall Shear Stress in Carotid Artery Stenting, Heliyon, **10**, No. 11 (2024).

[58] J. M. Zhang, L. Zhong, B. Su, M. Wan, J. S. Yap, J. P. Tham, ... & R. S. Tan, Perspective on CFD studies of coronary artery disease lesions and hemodynamics: a review, International journal for numerical methods in biomedical engineering, **30**, No. 6 (2014) 659-680.

[59] X. Zhang, Z. Jiao, Z. Hua, H. Cao, S. Liu, L. Zhang, ... & Z. Li, Localized elevation of wall shear stress is linked to recent symptoms in patients with carotid stenosis, Cerebrovascular Diseases, **52**, No. 3 (2023)
283-292.

[60] Y. Zhu, C. Armour, B. Li, S. Pirola, Y. Salmasi, T. Athanasiou, ... & X. Y. Xu, A combined 4D flow MR imaging and fluid–structure interaction analysis of ascending thoracic aortic aneurysms, Biomechanics and Modeling in Mechanobiology, (2025) 1-16.